



Apical oxygens and correlation strength in electron- and hole-doped copper oxides

Cédric Weber, Kristjan Haule, and Gabriel Kotliar

Department of Physics, Rutgers University, Piscataway, New Jersey 08854, USA

(Received 18 May 2010; revised manuscript received 12 August 2010; published 8 September 2010)

We use the local-density approximation in combination with the dynamical mean-field theory to carry out a comparative investigation of a typical electron-doped and a typical hole-doped copper oxide, NCCO, and LSCO, respectively. The parent compounds of both materials are strongly correlated electron systems in the vicinity of the metal to charge-transfer insulator transition. In NCCO the magnetic long-range order is essential to open a charge-transfer gap while Mott physics is responsible for the gap in LSCO. We highlight the role of the apical oxygens in determining the strength of the correlations and obtaining overall good agreement between theory and several experimentally determined quantities. Results for optical conductivity, polarized x-ray absorption, and angle-resolved photoemission are presented and compared with experiments.

DOI: [10.1103/PhysRevB.82.125107](https://doi.org/10.1103/PhysRevB.82.125107)

PACS number(s): 74.20.Fg, 71.10.Ca, 71.27.+a, 74.25.nd

I. INTRODUCTION

Since their discovery, the electronic structure of the high-temperature superconductors has been a subject of intensive theoretical attention as well as controversy, a situation that continues even today. A landmark question to understand these materials is how their physical properties follow from their electronic structure and to which extent simplified descriptions in the form of model Hamiltonians describe their basic physical properties in the normal state.

It is generally accepted that the physics of the copper oxide based high-temperature superconductor families is captured by the copper-oxygen layers and the relevant degrees of freedom are the copper $d_{x^2-y^2}$ orbitals and the oxygen p_x and p_y orbitals.^{1,2} Numerous studies have demonstrated that this model captures qualitatively the physics of the copper oxide planes. However, there have been several proposals that the $p_{\pm z}$ oxygen orbitals and the $d_{3z^2-r^2}$ copper orbital play an important role in the onset of orbital current order³ or for the existence of superconductivity.^{4,5}

Seeking a simpler low-energy description, several studies⁶ have shown that the Hubbard model describes some *qualitative* properties of the copper-oxygen layers. However, the precise energy range over which the description is valid and the quality of this description for different physical observables is still a subject of active research.

A related question is hence how to map the copper oxide layers onto the various effective Hamiltonians and what is the effective strength of the Coulomb correlations in these systems. There are various approaches tackling this issue, ranging from *ab initio* methods to model Hamiltonian studies.

The theoretical studies usually consist of a two-stage process: in the first step *ab initio* approaches use an approximate technique, such as constrained density-functional theory in the local-density approximation (LDA) or generalized gradient approximation, or quantum chemical methods, to derive the parameters and the form of the effective Hamiltonian.⁷⁻¹⁰

In the second step, model Hamiltonian-based approaches compute various observables in the framework of a given model Hamiltonian and given approximation technique. The parameters entering the model Hamiltonians are determined

by comparing the results side by side with experiment.

Numerous research efforts notwithstanding, even the basic question of the strength of the correlations in the copper oxide materials and the origin of the insulating gap in their parent compound has not been fully elucidated. There are two opposing physical pictures describing the origin of the insulating gap in these materials. In the so-called Slater picture, the insulating behavior is understood as the result of a doubling of the unit cell caused by antiferromagnetic (AF) long-range order. In the so-called Mott picture, the insulating behavior is the result of the local blocking of the electron propagation due to the strong Coulomb repulsion. In the latter picture, the insulating behavior originates from the localization of the electron and is not tied to any specific form of magnetic long-range order. Hence antiferromagnetic long-range order arises as a secondary instability. In the presence of magnetic long-range order, the unit cell is doubled and the two pictures, Slater and Mott, are continuously connected: no physical observable can provide a sharp distinction between the two, both magnetic order and blocking contribute to the insulating behavior. Mean-field theory treatments allow to study the paramagnetic (PM) state as an underlying *normal-state* mean-field solution, which can support a sharp transition between a paramagnetic metal and a paramagnetic insulator. This solution is not realized when other more stable mean-field solutions supporting long-range order exist, but within a mean-field framework, it can still be used to draw a sharp distinction between Slater insulators and Mott insulators by investigating if the ordered state is derived from a metallic or an insulating paramagnetic solution. The pioneering work of Zaanen Sawatzky Allen¹¹ and their sharp (so-called ZSA) boundary between charge-transfer metals and charge-transfer insulators can be viewed in this light.

A simple argument can be formulated for the Hubbard model to estimate the strength of the correlation of cuprates. Within a one band Hubbard description, parametrized by a bandwidth $W \approx 8t$ and a Coulomb repulsion U , the insulating gap of the paramagnetic insulator is $U - W$ and the superexchange is $J = 4t^2/U$. For cuprates, the gap is around ≈ 2 eV and $J \approx 0.1$ eV, and therefore it is found that the repulsion is of the order $U/W \approx 1.5$, which is above but not far from the Mott boundary $U \approx W$, and hence the cuprates are in a re-

gime of intermediate correlation strength. Conclusions on the placement of cuprates in a regime of intermediate correlation strength were also reached by numerical studies (for a review see, for example, Ref. 12).

The strength of the correlations was also studied in the three-band theory. In particular, large N slave boson mean-field theory of a three-band model (with no oxygen-oxygen transfer integrals)¹³ of the copper oxides obtained a sharp transition between the metal and the charge-transfer insulator in the paramagnetic phase. This metal-to-charge-transfer-insulator transition parallels the Brinkman Rice transition in the Hubbard model. It was found that there is indeed a correspondence between the two critical Coulomb repulsions of the Hubbard model U_{c1} (the minimal Coulomb repulsion that supports the paramagnetic insulator) and U_{c2} (the minimal repulsion that does not support a paramagnetic metal) with the two critical charge-transfer energies Δ_{c1} and Δ_{c2} , where the paramagnetic insulating state and the paramagnetic metallic state are destroyed, respectively. The critical value of the charge-transfer energy in the three-band theory (Δ_{c2}) plays the role of the critical U (U_{c2}) of the Hubbard model.¹³ Although a strong particle-hole asymmetry is expected in the three band theories, since doped electrons reside mainly on copper sites while doped holes reside mainly on the oxygen sites, it was shown that the resulting quasiparticle band structure was surprisingly particle-hole symmetric. Indeed, it is due to the strong copper-oxygen hybridization which results in the formation of Zhang-Rice (ZR) singlets and to the quasiparticles that involves copper spin and oxygen charge.

Other more realistic treatments of the three-band description of the copper oxides were carried out within the slave boson framework. Some include the oxygen dispersion,^{14,15} additional copper and oxygen orbitals,¹⁶ short-range magnetic correlations,^{17,18} the nearest-neighbor Coulomb interactions,¹⁹ or the electron phonon coupling.²⁰ Within slave boson mean-field theory of the three-band model, the parent compound of hole-doped cuprates LSCO was located close but above (i.e., on the insulating side of) the metal-to-charge-transfer-insulator transition boundary.²¹

The development of dynamical mean-field theory²² (DMFT) and their extensions²³⁻²⁵ opened new avenues to advance our qualitative understanding of the electronic structure of the cuprates and its quantitative description. DMFT goes beyond slave bosons theories: this method treats both coherent and incoherent features on the same footing, whereas slave bosons theories are not able to capture the coherent character of the physical solution. DMFT successfully describes the Mott transition of the Hubbard model and gives a deeper understanding of the Brinkman-Rice transition.^{22,26} Single-site DMFT calculations can also be extended to more precise cluster calculations. In particular, cluster corrections in DMFT allow to assess the validity of the single-site calculations.

The question of the strength of the correlations was also addressed by DMFT studies of multiband model Hamiltonians for the copper oxides planes.^{27,28} The phase diagram with respect to the charge-transfer energy and the Coulomb repulsion of the copper orbitals was studied. The boundary between the metallic and the charge-transfer-insulator solutions was located, as well as the crossover line between the

charge-transfer-insulator and the Mott insulator. A full phase diagram of a copper oxide model and a very complete analogy with the DMFT studies of the Mott transition in the Hubbard model was also performed recently.²⁹

Combination of DMFT with electronic-structure methods, such as LDA, allows to combine the *ab initio* and the model Hamiltonian viewpoint in the LDA+DMFT framework. The LDA+DMFT method²³ allow, in particular, to determine the strength of correlations for specific materials, such as NCCO and LSCO, and there are still several important issues unresolved regarding how this picture is connected to the cuprates: (a) how should the different materials be placed in the qualitative ZSA phase diagram. Should the parent compounds of the copper oxide materials be thought as Slater or Mott/charge-transfer insulators, (b) what significant differences are there in the different level of description, mainly what are the differences between the one-band and three-band theory, (c) what is the quality of the description of the various experimental observables, for the different low-energy models involving a different number of bands, and finally (d) can one obtain a consistent picture of the spectroscopies of hole- and electron-doped cuprates using a first-principles method.

In regards to point (a), the issue is still under debate. Using the analysis of model Hamiltonians, Refs. 29 and 30 classify the parent compounds of electron- and hole-doped compounds as Slater insulators in the metallic side of the ZSA phase diagrams. Previous LDA+DMFT studies classified LSCO (Ref. 31) as a Mott insulator (or more precisely as a charge-transfer insulator) and NCCO (Ref. 32) was identified as Slater insulator. On the other hand, the first-principles study of Ref. 33 found NCCO's parent compound to be Mott insulator. Finally, the phenomenological analysis of experimental data in Ref. 34 concludes that the analysis of the optical data requires comparable strength of interactions in hole- and electron-doped cuprates.

In regards to point (b) the energy range over which the spectral functions of the three-band model are reproduced by the one-band model is also subject of controversy. For example, Refs. 29 and 30 assert that the three-band model and a one-band model of the copper oxides are quantitatively equivalent up to a scale of 4 eV while a similar analysis by Macridin *et al.*³⁵ concludes that the range of validity of the Hubbard model is much smaller and is on the order of 0.5 eV. An additional controversy, regarding the differences between the one-band and the three-band theory, is connected to the values of the insulating gap in the paramagnetic insulator. In particular, in a one-band theory near U_{c2} , the gap of the paramagnetic solution is substantially smaller than the gap of the antiferromagnetic solution for the same parameters.^{30,36,37} This is not the case in the three-band model where antiferromagnetism increases the value of the paramagnetic insulating gap by less than 15%.³¹ The latter statement is controversial with respect to Ref. 29, which argued that the one-band model and the three-band model are similar in their physics up to energies as large as twice the gap.

Regarding point (c), many authors used the theoretical results obtained with the Hubbard model to fit experiments. For instance Ref. 38 considered a treatment of the Hubbard

model with variational cluster perturbation theory. It could match experiments but it required a sensible dependence of the Hubbard U on the level of doping. On the other hand, an approximate diagrammatic treatment of the one-band model³⁹ indicates that the experimental optical spectra and the dispersion^{40,41} can be reproduced without a doping-dependent U .

Note that a three-band LDA+DMFT study was able to describe the experimental data of NCCO without having to invoke doping-dependent parameters.³² Moreover, using the same technique, a successful description of both the integrated optical weights and the magnitude of the optical conductivity below the charge-transfer gap for LSCO and NCCO was obtained.³¹ This approach however does not give the correct magnitude of the optical conductivity of LSCO for energies on the order of the charge-transfer gap, suggesting that additional orbitals might play an important role in LSCO.

In this paper we reconsider these issues building on our earlier work of Refs. 31 and 32. We use an *ab initio* approach, e.g., the local-density approximation combined with the dynamical mean-field theory²³ to study the electronic structure of NCCO and LSCO. The comparative study of two typical cuprate compounds LSCO and NCCO allow us to place firm bounds ascertaining the importance of correlations in the cuprates. The good agreement between theory and experiments, achieved using single-site LDA+DMFT within a multiband framework, for two different compounds, is a significant results and illustrates the power of this new first-principles approach to correlated materials. Our results contrast with a recent phenomenological analysis of optical data, of electron and doped cuprates: they concluded that for a one-band theory, vertex corrections beyond single-site DMFT were required to obtain a reasonable fit to experiments.³⁴

In this work, we include also the apical oxygens and an additional copper orbital ($d_{3z^2-r^2}$), which were not included in our previous study of LSCO.³¹ This extends the quantitative agreement between theory and experiments to a broader energy range. It sheds light on why the three-band model description of NCCO (Ref. 32) agrees with experiments up to larger energy scales than for LSCO.³¹ NCCO, in the T' structure, lacks apical oxygens and is therefore well described by the three-band model up to a much higher energy scale, justifying the excellent agreement between theory and experiment found in Ref. 32.

We confirm that for integration cutoffs smaller than half the gap of the parent compound, the additional apical oxygen degrees of freedom do not affect the integrated optical weights in LSCO. This validates the analysis carried out in Ref. 31 to extract the strength of correlations in these materials, which was based on analysis up to an energy scale of half the charge-transfer gap, i.e., 1 eV. The apical oxygens however substantially affect the shape of the optical conductivity and it strongly modifies the optical conductivity of LSCO around 2 eV. While the hole occupancy of the p_z orbital is small, it has a clear effect on the optical conductivity of the hole-doped cuprates. We show here that within the first-principles LDA+DMFT framework, extensions of the model to include further orbitals or longer range correlations

(using cluster extension) consistently improves precision of the calculation and improves agreement with experiments.

The organization of our paper is the following. In Sec. I we describe the phase diagram of NCCO and LSCO within single-site and two-site cluster DMFT, and highlight the role of magnetic order and singlet correlations in these materials. In Sec. II we present the evolution of the angle-resolved photoemission spectra (ARPES) of these materials, stressing the various features of the theory that require a description beyond static mean-field theory and its comparison with the experiments. Details regarding the formula used in Sec. II to compare the spectral weight with experiments are given in Appendix A. Section III focuses on the optics and how the evolution of the optical properties with doping and temperature in NCCO and LSCO can be understood as the result of placing the two compounds on two different sides of the ZSA boundary, once the band structure of both materials is taken into account. The inclusion of the apical oxygens in the theoretical modeling is important to obtain correct results for various physical quantities, including the shape of the optical conductivity and the integrated optical spectral weights with a cutoff on the order of the charge-transfer gap. We also discuss the connection of the optical conductivity with various features in the ARPES spectra and compute the occupation of the different orbitals which are relevant to the x-ray absorption spectroscopy (XAS) spectra. There is one parameter, the double-counting correction, whose determination in the LDA+DMFT approach is not unique. We thus examined in the last section the dependence of our results on this parameter and used this dependence to estimate the proximity of both NCCO and LSCO to the ZSA boundary. The tight-binding parametrization obtained makes contact with model Hamiltonian studies and is reported in Appendix B. We conclude with some outlook for further work.

II. FORMALISM

LDA+DMFT uses first-principles density-functional theory methods to extract the hopping parameters of the model, which is subsequently solved using DMFT and its extensions. The LDA calculation was carried out with the PWSCF package,⁴² which employs a plane-wave basis set and ultrasoft pseudopotentials.⁴³ Downfolding to a three-band model, containing copper $d_{x^2-y^2}$ and two oxygen p_σ orbitals was performed by the maximally localized Wannier functions method.^{44,45} The downfolded LDA band structure of Nd_2CuO_4 (NCCO) and La_2CuO_4 (LSCO) (see Appendix B) results in the following three-band Hamiltonian:

$$\mathcal{H}_t = \sum_{ij\sigma, (\alpha, \beta) \in (p_x, p_y, d_{x^2-y^2})} t_{ij}^{\alpha\beta} c_{i\alpha\sigma}^\dagger c_{j\beta\sigma} + \epsilon_p \sum_{i\sigma\alpha \in (p_x, p_y)} \hat{n}_{i\alpha\sigma} + (\epsilon_d - E^{\text{dc}}) \sum_{i\sigma} \hat{n}_{id\sigma}, \quad (1)$$

where i and j label the CuO_2 unit cells of the lattice, and $t_{ij}^{\alpha\beta}$ are the hopping matrix elements. ϵ_d and ϵ_p are the on-site energies of the d and p orbitals, respectively. Finally, we note that the charge-transfer energy $\epsilon_d - \epsilon_p$ plays the same role as U in the single-band Hubbard model, as seen, for example, in slave bosons mean-field studies.²¹

TABLE I. LDA band calculations give us different set of parameters for LSCO, NCCO, and PCCO compounds. The f states of the Nd and Pr atoms have been treated as core states and are not treated as valence state. Long-range hoppings (not shown) are also considered within the calculations. The amplitude of the nearest-neighbors hoppings (t_{pp}, t_{dp}), the LDA on-site energies ($\epsilon_p^0, \epsilon_d^0$) and the on-site repulsion U_d are shown in this table in eV. In electron notations the bonding orbitals enter the Hamiltonian with a negative transfer integral sign, and the antibonding orbitals with a positive sign.

Compound	$\epsilon_d^0 - \epsilon_p^0$ (eV)	U_d (eV)	t_{dp} (eV)	t_{pp} (eV)
NCCO (this work)	1.61	8	1.16	0.54
PCCO (this work)	1.65	8	1.17	0.54
LSCO (this work)	2.76	8	1.41	0.66
NCCO (Ref. 46)	1.42	10	1.18	0.69
LSCO (Ref. 46)	0.918	10	1.357	0.841
LSCO (Ref. 9)	3.5	7.9	1.5	0.6
LSCO (Ref. 10)	3.6	10.5	1.3	0.65

To this Hamiltonian, we add the on-site Coulomb repulsion U on the $d_{x^2-y^2}$ orbital

$$\mathcal{H}_U = U_d \sum_i \hat{n}_{id\uparrow} \hat{n}_{id\downarrow}, \quad (2)$$

where the value of $U_d = 8$ eV. The LDA+DMFT method, accounts for the correlations which are included in both LDA and DMFT by a double-counting correction to the d -orbital energy, $E_{dc} = U_d(n_d - 0.5)$, which amounts to a shift of the relative positions of the d and p orbitals. Here we take n_d to be the occupancy of the correlated orbital in the parent compound, which gives the double-counting corrections $E_{dc} = 4.8$ eV (3.12 eV) for NCCO (LSCO).

The LDA downfolded parameters are shown in Table I, which we find to be close to those extracted by other first-principles methods. An extended six-band model, that considers the $d_{3z^2-r^2}$, p_z , and p_{-z} orbitals, was also considered for LSCO. The six-band Hamiltonian is

$$\begin{aligned} \mathcal{H}_{apical} = & \sum_{ij\sigma, (\alpha, \beta) \in (p_x, p_y, p_{\pm z}, d_{x^2-y^2}, d_{3z^2-r^2})} t_{ij}^{\alpha\beta} c_{i\alpha\sigma}^\dagger c_{j\beta\sigma} \\ & + \sum_{i\sigma, \alpha \in (p_x, p_y, p_{\pm z})} \epsilon_\alpha \hat{n}_{i\alpha\sigma} \\ & + \sum_{i\sigma, \alpha \in (d_{x^2-y^2}, d_{3z^2-r^2})} (\epsilon_\alpha - E^{dc}) \hat{n}_{i\alpha\sigma} \\ & + U_d \left(\sum_{i, \alpha \in (d_{x^2-y^2}, d_{3z^2-r^2})} \hat{n}_{id\uparrow} \hat{n}_{id\downarrow} + \sum_i \hat{n}_{id_{x^2-y^2}} \hat{n}_{id_{3z^2-r^2}} \right). \end{aligned} \quad (3)$$

The hopping parameters t_{ij} were obtained by downfolding the LDA band structure to six orbitals ($d_{x^2-y^2}$, $d_{3z^2-r^2}$, p_x, y , and $p_{z,-z}$). The double counting for the six-band model is defined as $E_{dc} = U_d(n_{d_{x^2-y^2}} + n_{d_{3z^2-r^2}} - 0.5)$. The same on-site repulsion U_d was considered for the $d_{x^2-y^2}$ and $d_{3z^2-r^2}$ orbitals.

We solve these models using DMFT in which the Green's function is given by⁴⁷

$$\mathbf{G}_k(i\omega_n) = (i\omega_n + \mu - \mathbf{H}_k - \mathbf{\Sigma}(i\omega_n))^{-1}, \quad (4)$$

where \mathbf{H}_k is the Fourier transform of the \mathcal{H}_i in Eqs. (1) and (3). $\mathbf{\Sigma}$ is the self-energy matrix being nonzero only in the d orbital. The self-energy in Eq. (4) is obtained by solving an Anderson impurity model subject to the DMFT self-consistency condition,

$$[i\omega - E_{imp} - \mathbf{\Sigma}(i\omega) - \mathbf{\Delta}(i\omega)] = \hat{P} \left[\frac{1}{N_k} \sum_{\mathbf{k} \in \text{BZ}} G_{\mathbf{k}}(i\omega) \right]^{-1}, \quad (5)$$

where the sum runs over the first Brillouin zone (BZ) and \hat{P} is projecting the averaged Green's function onto the impurity-cluster subspace.

In this work we use the continuous time quantum Monte Carlo impurity solver algorithm.^{48,49} Real frequency resolved quantities were obtained by analytic continuation of the observables obtained in Matsubara frequencies. We have crossed checked the analytic continuation of the observables obtained on the Matsubara axis using several other numerical solvers: the exact diagonalization (ED) solver,²² the density-matrix renormalization-group (DMRG) solver,⁵⁰ and the NCA solver (noncrossing diagram approximation). Continuous time quantum Monte Carlo (CTQMC) and ED/DMRG/NCA are complementary tools, working, respectively, on the Matsubara and real axis.

Magnetism was considered within the single-site DMFT by solving two independent impurity problems while in the case of the two-site cluster DMFT (c-DMFT), the two-site magnetic unitcell is mapped to a two-impurity cluster. Cluster DMFT improves single-site DMFT by adding the nonlocal self-energy, not present in the single-site DMFT. The six-band calculation maps the two-correlated orbitals $d_{x^2-y^2}$ and $d_{3z^2-r^2}$ to an impurity containing two different orbitals.

Finally, model Hamiltonians (1) and (2) were studied previously (for example, see Refs. 27 and 28). When U_d is large, there is a metal to charge-transfer insulator transition at integer filling, as a function of the charge-transfer energy $\epsilon_d - \epsilon_p$. However the electron-doped cuprates fall in a regime where the phases with magnetic long-range order occupy a large fraction of phase space and this regime was not investigated previously.

III. PHASE DIAGRAM OF LSCO AND NCCO

In this section we discuss the phase diagram of NCCO and LSCO and, in particular, their magnetic properties. We compare the various treatments of the short-range and long-range correlations. In particular, we consider the ordered state within the single-site DMFT and within the two-site cluster DMFT.

In Fig. 1(a) we show the magnetic moments of NCCO obtained within a three-band description (left panel of Fig. 1). Single-site DMFT data of NCCO (blue circles, left panel) are in remarkable agreement with experimental data for all dopings,⁵¹ though LDA+DMFT slightly overesti-

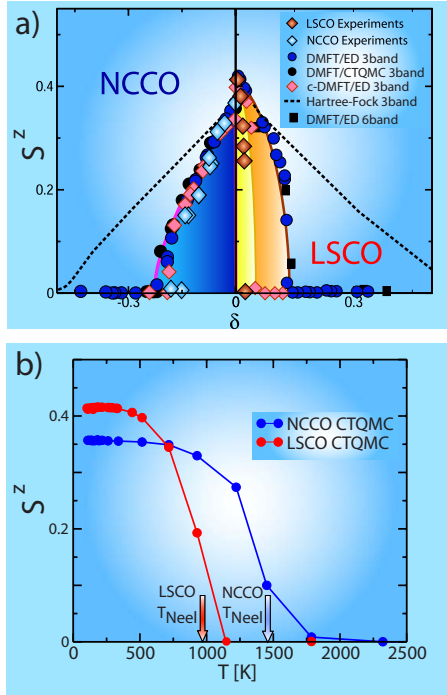


FIG. 1. (Color online) (a) We show the theoretical mean value of the staggered magnetization $S^z = \frac{1}{2}(n_{\uparrow} - n_{\downarrow})$ obtained for LSCO and NCCO by both single-site DMFT (LDA+DMFT) and cluster cellular DMFT (LDA+cDMFT) of the three-band theory, and DMFT of the six-band theory. Experimental values $M(\delta)/M_0 (M_0 = M(\delta=0))$ for NCCO (Ref. 51) and LSCO (Ref. 52) are also shown, and for comparison with DMFT, we assume $M_0 = M_{\text{DMFT}}(\delta=0)$, where M_{DMFT} is the magnetic moment at 0 doping obtained by single-site DMFT. The general trend compare well to our data, and for NCCO we obtain a qualitative agreement for the critical doping. For LSCO we find that the magnetization vanishes at large doping within the single-site DMFT approximation but when the possibility of local singlet is allowed (cDMFT) the range of stabilization of the long-range order is much reduced. Note that the theoretical magnetic moment was obtained at constant temperature $T=89$ K, and experimentally at 2 K for LSCO and 8 K for NCCO. (b) Magnetization versus temperature in the parent compounds of NCCO and LSCO obtained by single-site DMFT for the three-band theory. The extracted mean-field Neel temperature is about 1500 K for NCCO and 1000 K for LSCO.

mates the range of stabilization of the Neel state: in experiment, the magnetic order of NCCO vanishes at doping $\delta \approx 0.15$ while in our calculations we find a slightly larger critical doping of $\delta \approx 0.2$. We also show data for the cluster cellular DMFT (LDA+cDMFT) (gray diamonds). For NCCO, the c-DMFT and the single-site DMFT data are almost identical. This is a very strong test that the magnetic correlations of NCCO are well captured by single-site DMFT.

In the case of LSCO (right panel of Fig. 1), we found significant difference in the region of stability of the magnetic state between the single-site and cluster DMFT ($\delta < 10\%$), hence the dynamical short-range correlations—absent in single-site approach—are very important for LSCO in the underdoped regime, as reported in Ref. 18. For LSCO, we also considered the six-band theory (the six-band

calculations include the description of the $p_{\pm z}$ and $d_{3z^2-r^2}$ orbitals), which does not change the magnetic moment of the three-band theory. Experimental values for LSCO (Ref. 52) are also shown and compare qualitatively to our data.

We also carried out the Hartree-Fock calculation, and we found that in this static approach the magnetization vanishes only at unrealistic large doping $\delta \approx 50\%$ for both NCCO and LSCO [dashed line in Fig. 1(a)], which points toward the important role of dynamic correlations at finite electron and hole dopings. Indeed, in the Hartree-Fock calculations, the picture is fairly simple: The magnetic state is stabilized due to an optimization of the Coulomb energy at the expense of the kinetic energy (the staggered magnetic order avoids double occupation) and in this picture there is no strong difference between LSCO and NCCO, as shown in Fig. 1(a). The same mechanism is responsible for slight overestimation of the critical doping within DMFT.

When comparing to experiments, it is important to keep in mind that two-dimensional compounds are not able to sustain infinite-range magnetic order at a finite temperature (Mermin-Wagner theorem⁵³). Therefore, the Neel temperature within DMFT should be interpreted as the temperature below which the magnetic correlations become long but remain finite. This temperature can be much higher than the actual Neel temperature of the material, which is controlled by the magnetic exchange between the two-dimensional copper oxide layers; and vanishes for a well-separated copper oxide planes.

In Fig. 1(b) we show the temperature dependence of the magnetic moment for the three-band calculations of LSCO and NCCO. The extracted mean-field Neel temperature is about 1500 K for NCCO and 1000 K for LSCO, which is much higher than the experiment Neel temperature. Finally, we emphasize that the magnetic moment of the parent compound of LSCO $m=0.42$ is larger than the one of NCCO $m=0.35$, which might suggests that LSCO is more correlated than NCCO. The strength of the correlations can also be quantized by calculating the quasiparticle renormalization amplitude Z (see Fig. 2). First, we consider the paramagnetic solutions of both NCCO (white circles on the left side) and LSCO (blue circles on the right side). We find that the quasiparticle weight is going to zero in the parent compound of LSCO: This is a signature that LSCO is a charge-transfer insulator. For NCCO, we find that it is going to a finite value at zero doping, which is the signature that NCCO is a paramagnetic metal.

At finite doping, we find that the quasiparticle weight of the paramagnetic state is much larger in NCCO than in LSCO. This is a signature that NCCO is more metallic and less correlated than LSCO.

We now turn to the calculations for the ordered state of both LSCO (red circles on the left) and NCCO (red diamonds on the right). Here the average quasiparticle weight in the ordered state was obtained by the following formula: $Z = \sum_i \rho_i(\epsilon_F) / \sum_i \frac{\rho_i(\epsilon_F)}{Z_i}$. The motivations comes from the formula for the specific heat of the magnetic system given by $\gamma_i \propto \frac{\rho_i}{Z_i}$ with $i=A, B$.

The quasiparticle weight in the ordered state of NCCO is larger than the one for LSCO, which shows that the ordered

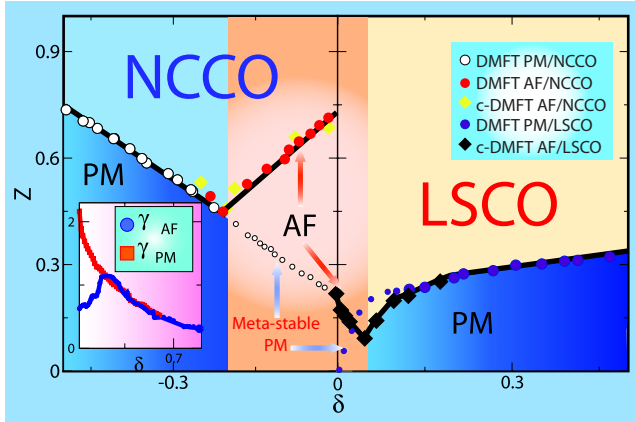


FIG. 2. (Color online) We show the quasiparticle weight Z for the three-band description of LSCO and NCCO. The quasiparticle weight of the PM is finite at integer filling for NCCO, which is a signature that the paramagnetic state of NCCO is a metal. In the ordered state of NCCO (AF), the quasiparticle weight is estimated by the specific heat of the A and B magnetic sublattices $\gamma_i \propto \frac{\rho_i(\epsilon_F)}{Z_i}$ and $i=A,B$, and the total quasiparticle weight Z is given by $Z = \sum_i \rho_i(\epsilon_F) / \sum_i \frac{\rho_i(\epsilon_F)}{Z_i}$. The specific heat γ of the AF and PM states of NCCO are shown in the inset.

state of NCCO is also less correlated than LSCO, and hence the character of the paramagnetic state of the parent compounds (paramagnetic metal versus paramagnetic insulator) has direct consequences for the magnetic solutions.

We find that the mechanism to open a gap at integer filling is totally different for hole- and electron-doped compounds, and our results place NCCO and LSCO to different regions of the ZSA phase diagram. For hole-doped compound NCCO, the quasiparticles are scattered increasingly and get a very short lifetime when approaching the insulator (charge-transfer insulator). In the electron-doped compound NCCO, the system minimizes its free energy by doubling the unit cell which opens a Slater gap (Slater insulator).

We note that the presence of magnetism is concomitant with an entropy loss, which results in an increase in the quasiparticle weight. The direct consequence is that the specific heat γ of the ordered state is lower than the specific heat of the paramagnet (inset of Fig. 2).

Finally, our results reproduce the striking asymmetry in the experimental magnetic phase diagrams of NCCO and LSCO. We emphasize that the difference in correlation strengths for NCCO (Slater insulator) and LSCO (charge-transfer insulator) is an essential ingredient of our theory to correctly capture the asymmetry of the cuprates magnetic phase diagram. Note that in our theory this difference in correlation strength comes from difference in charge-transfer energy and not from the difference in the copper Coulomb repulsion.

The asymmetry between particle and hole doping was also investigated by cluster DMFT in the one-band Hubbard model^{54–56} and in the Anderson lattice.⁵⁷ In the one-band Hubbard model, it was also found that doping with electron and holes leads to somewhat different phase diagrams. We emphasize that in these cluster DMFT studies,^{54–56} the electron- and the hole-doped sides of the phase diagram were

modeled with different band parametrization but with the same value of the Coulomb repulsion U , which in the context of the single-band model, leads to the same correlation strength. In this work, we observe that in addition to the differences in the band parametrizations, there is also a fundamental difference between NCCO and LSCO that derives from their difference in correlation strengths.

IV. PHOTOEMISSION AND FERMI SURFACE OF NCCO

The basic quantity describing the electronic structure of the material is the electronic spectral function,

$$A^\alpha(\mathbf{k}, \omega) = -\frac{[\text{Im } \mathbf{G}(\mathbf{k}, \omega)^{\alpha, \alpha}]}{\pi}, \quad (6)$$

where α is the orbital index and \mathbf{k} is running through the unfolded Brillouin zone. The total spectral weight is $A(\mathbf{k}, \omega) = \sum_\alpha A^\alpha(\mathbf{k}, \omega)$. Experiments like ARPES are able to probe the k -dependent spectral functions and can therefore be compared side-by-side with theoretical calculations.⁵⁸ In this section we investigate the agreement between the theoretical spectra and ARPES measurements.

In Figs. 3(a), 3(c), and 3(e) we show the spectral functions resolved in momentum space. In Figs. 3(b), 3(d), and 3(f) we show the integrated spectral functions that show the energy locations of the main spectral features. In the parent compound [Figs. 3(a) and 3(b)], we find two dispersive peaks separated by the charge-transfer gap of about 1.2 eV, as expected in NCCO.⁵⁹

The spectral feature below the Fermi level [Fig. 3(b)] is an admixture of oxygens and copper orbitals, commonly known as the ZR singlet. It is worth noting that our results show that the oxygens orbitals carry no magnetic moment. The oxygen sites average the magnetization on its both copper neighbors.

When the Slater gap opens, there is a spectral weight transfer from the upper Hubbard band (UHB) to the Zhang-Rice singlet and the lower Hubbard band (LHB) (located at -10 eV, not shown), such that minority spectral weight is concentrated in the UHB, and the majority spectral weight is mostly present in the LHB and in the ZR singlet.

The top of the lower band occurs at $(\pi/2, \pi/2)$ while the bottom of upper band appears at $M=(\pi, 0)$, therefore the gap is indirect (see yellow arrow in panel a). Those two bands can also be obtained in the simpler Hartree-Fock approximation, though the size of the gap is overestimated in a static mean field.

At 10% electron doping [Figs. 3(c) and 3(d)], NCCO is still magnetic, and therefore the Zhang-Rice singlet and the upper Hubbard band are well separated. Those two features are also observed by the simpler Hartree-Fock approximation. What is clearly not visible in static mean field is the presence of a very sharp and narrow band slightly below and above the Fermi level [Fig. 3(c)] that corresponds to the quasiparticle peak (QP) in the integrated spectra [Fig. 3(d)]. It is worth noting that the optical transitions occur at this doping within these narrow bands, from the narrow band below the Fermi level to the narrow band above the Fermi level, as depicted in Fig. 3(c) by the vertical arrow. In the

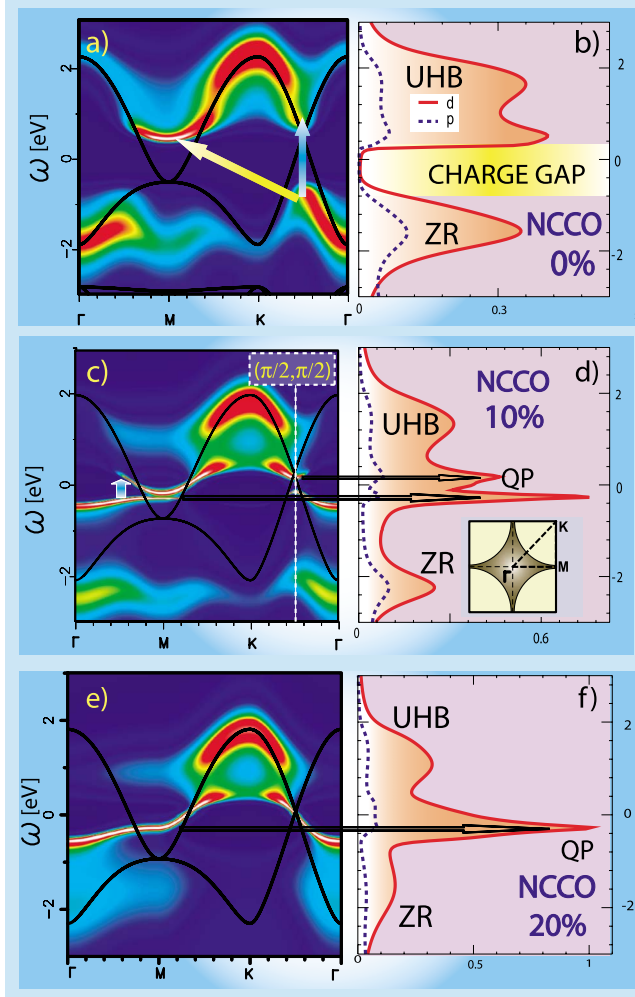


FIG. 3. (Color online) Frequency-dependent spectral weight $A(k, \omega)$ obtained by LDA+DMFT of NCCO at (a) integer filling, (c) 10% and (e) 20% electron doping for NCCO. $A(k, \omega)$ was obtained along the usual path Γ -M-K- Γ in the Brillouin zone (see inset of d). The solid lines are the rigid LDA bands. The partial density of states of the d and p orbitals are shown in (b), (d), and (f). The density of states is showing the UHB, the ZR singlet and the QP for the doped compounds. (a) At integer filling, we find for NCCO that the indirect gap is ≈ 1.2 eV, between $(\pi, 0)$ and $(\pi/2, \pi/2)$, as shown by the diagonal arrow, and the direct gap is about 1.5 eV, as indicated by the vertical arrow. (d) At 10% doping we observe a splitting of the quasiparticle peak due to magnetism. The splitting of the quasiparticle peak is associated with the magnetic pseudogap at $(\pi/2, \pi/2)$ in panel (c). The horizontal arrows pointing from (c) to (d) are guide to the eyes. The optical transitions at 10% doping occur around $(\pi, 0)$ within the quasiparticle band, as indicated by the vertical arrow. (e) At 20% doping, magnetism is destroyed and the pseudogap at $(\pi/2, \pi/2)$ is closed. The quasiparticle peak in panel (f) is clearly related to the spectral weight close to the Fermi surface at $(\pi, 0)$, as indicated by the horizontal arrow.

ordered state of NCCO we observe in the ordered phase a splitting of the quasiparticle peak [Fig. 3(d)] into two structures. The first corresponds to the narrow band below the Fermi level, and its main weight is at $M=(\pi, 0)$, as indicated by the lower horizontal arrow. The peak slightly above the Fermi level is due to the spectral weight at $\mathbf{k}=(\pi/2, \pi/2)$

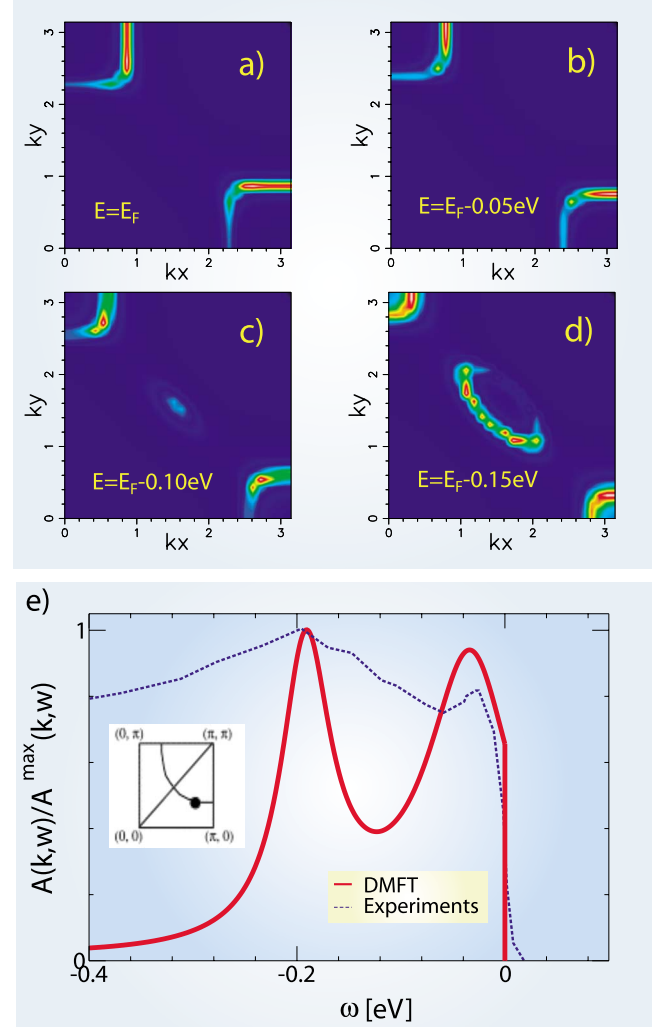


FIG. 4. (Color online) Fermi-surface maps obtained by DMFT calculations in the ordered state at 10% doping, (a) at the Fermi energy and (b)–(d) at lower energies ranging from -0.05 to -0.15 eV. The Fermi-surface map at the Fermi level is shaped by the presence of magnetism, whereas the arc in the energy map at energy -0.15 eV is also present in the paramagnetic calculations. (e) comparison of $A(\omega)$ for a fixed k point $k=(3\pi/4, \pi/4)$ (shown in the inset) obtained theoretically (lower curve) and experimentally from Ref. 60 (upper curve). The peak at -0.03 eV is due to magnetism, and the peak at lower energy -0.2 eV is associated to the arcs seen in (d).

(see upper horizontal arrow) and is related to the pseudogap around $\mathbf{k}=(\pi/2, \pi/2)$.

Upon larger doping 20% [Figs. 3(e) and 3(f)], magnetism disappears and the pseudogap at $\mathbf{k}=(\pi/2, \pi/2)$ closes. The peak slightly above the Fermi level, that was present at 10% doping, now disappears.

We now turn to Figs. 4(a)–4(d), where we show the spectral functions resolved in momentum space at fixed energies E_f , $E_f-0.05$ eV, $E_f-0.1$ eV, and $E_f-0.15$ eV at finite doping 10%. At this doping NCCO is magnetic. The magnetic Fermi surface in panel (a) has a squarelike shape structure centered around $M=(\pi, 0)$. At lower energy, in panel d, we observe the presence of an arc centered around

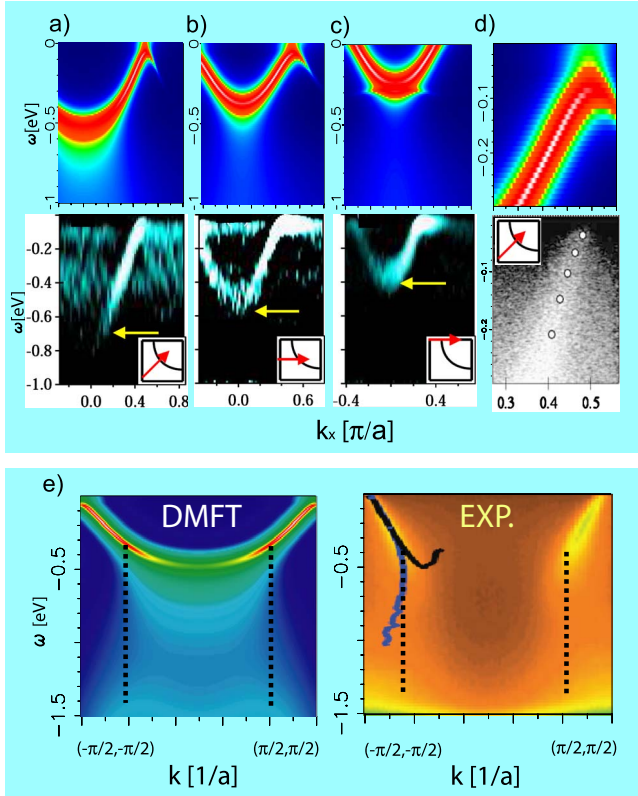


FIG. 5. (Color online) Side-by-side comparison of $A(k, \omega)$, along the path as depicted in the inset, obtained theoretically (upper row) and experimentally (lower row), (a)–(c) at 15% electron doping from Ref. 61, and (d) at 13% doping from Ref. 60. (e) Comparison between DMFT (left side) and experiments of Ref. 62 (right side), along the nodal cut of the Brillouin zone at 17% electron doping. The agreement between DMFT and experiments is remarkable. The vertical dashed lines are guide to the eyes to illustrate the presence of a sharp kink in the dispersion (waterfall).

$\mathbf{k}=(\pi/2, \pi/2)$. This comes primarily from the pseudogap around momentum point $\mathbf{k}=(\pi/2, \pi/2)$, which is a signature of the magnetic long-range order (the Fermi surface of the ordered state is gapped at $\mathbf{k}=(\pi/2, \pi/2)$). The Fermi surface of the ordered state moves toward the usual Fermi arc shape when the system becomes metallic and the pseudogap at $\mathbf{k}=(\pi/2, \pi/2)$ is closed in the paramagnet.

Some aspects of the doped electronic structure can be understood in terms of the Hartree-Fock rigid-band picture, for example, the holes appear first upon doping at the $M=(\pi, 0)$ point, but the renormalization of the bands, and the multiple peak structure in energy for a given momentum point [see Fig. 4(e)] are not captured in static mean field.

In Fig. 4(e) we show the energy dependence of the spectral function at a fixed \mathbf{k} point (shown in the inset of the figure). The peak close to the Fermi energy is connected to the squarelike Fermi surface of panel (a) and is hence connected to magnetism. The peak at lower energy -0.2 eV is related to the arc shape of panel (d) and has paramagnetic character. The peak positions are in a very good agreement with recent angle-resolved photoemission measurements of Ref. 60 also shown in Fig. 4(e).

In Fig. 5(a)–5(c) we compare side-by-side experimental

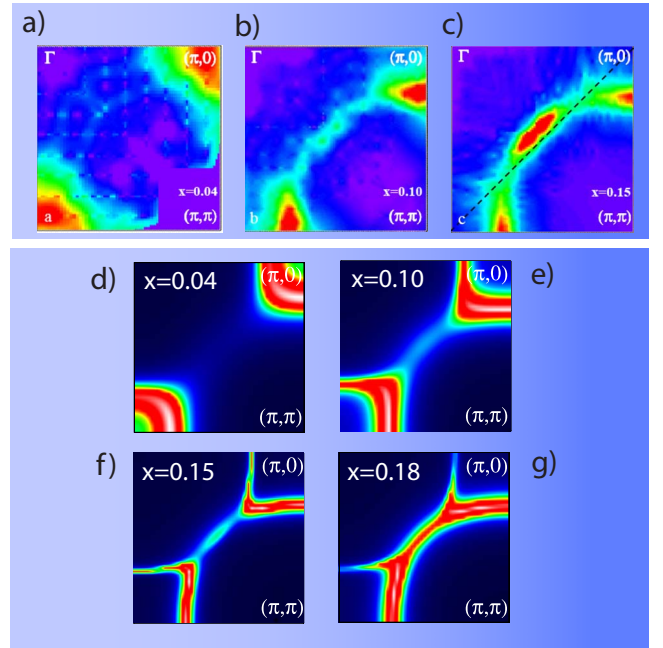


FIG. 6. (Color online) Side-by-side comparison of the Fermi surface obtained experimentally (reproduced from Ref. 63) and obtained by single-site DMFT calculations for NCCO in the ordered state. (a) Experimental results for doping 4%, (b) for 10% electron doping, and (c) 15% electron doping. The results are compared to DMFT calculations for similar dopings (d)–(g). The Fermi surface at low doping (a) is centered around $M=(\pi, 0)$ and is moving toward the Fermi arc shape (g) when magnetism is destroyed.

data (middle panels)⁶¹ and DMFT calculations (upper panels). The agreement is quantitative showing that our approach captures the low-energy physics of NCCO. The pseudogap at $(\pi/2, \pi/2)$ is also observed in experiments⁶⁰ [Fig. 5(d), middle panel] in the ordered phase and compares well to our theoretical calculations [Fig. 5(d), upper panel]. In Fig. 5(e) we show the spectral weight along the diagonal cut of the Brillouin zone. We observe the presence of a sharp kink in the dispersion (*waterfall*) that was also recently reported in experiments.⁶²

In Fig. 6 we show the doping evolution of the Fermi surface obtained by theoretical calculations (lower panels). We find that upon doping, the Fermi surface moves from the squarelike magnetic Fermi surface toward the Fermi arcs of the paramagnetic Fermi surface (panels d–g). This is explained by the closing of the pseudogap at $\mathbf{k}=(\pi/2, \pi/2)$. The agreement with experiments (panels a–c)⁶³ is very satisfactory.

V. PHOTOEMISSION OF LSCO

In this section we focus on the spectral functions of LSCO. In particular, we focus on the six-band theory, which includes $d_{3z^2-r^2}$ and $p_{\pm z}$ orbitals, which are expected to play a role in LSCO, due to the presence of apical oxygens. Note that the apical oxygens are absent in NCCO.

In Fig. 7(a) we show the momentum resolved spectral function of LSCO obtained by DMFT. We observe a direct

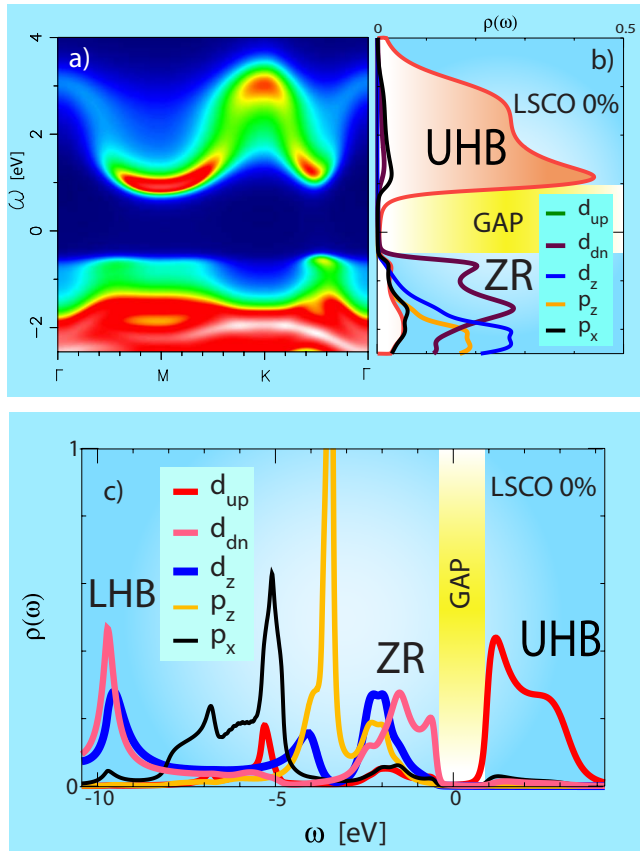


FIG. 7. (Color online) (a) Frequency-dependent spectral weight $A(k, \omega)$ obtained by LDA+DMFT of a six-band model description of the parent compound of LSCO. (b) Partial density of states of the $d_{x^2-y^2}$, $d_{3z^2-r^2}$, $p_{(x,y)}$, and $p_{\pm z}$ orbitals. We observe a direct gap of 1.8 eV in LSCO. Notice that the spectral weight is very incoherent close to the Fermi energy in the lower band. (c) Partial density of states on a larger energy scales. The LHB is located at a very low energy -10 eV, and the UHB is also shown. The $d_{3z^2-r^2}$ and $p_{\pm z}$ orbitals have a strong weight between -4 and -1 eV.

gap ≈ 1.8 eV, which is larger than the gap in NCCO, showing that LSCO is more correlated than NCCO. The partial density of states [Fig. 7(b)] shows two dispersive features, the UHB and a the band below the Fermi level, the ZR singlet. The latter is an admixture of oxygen and copper characters. The Zhang-Rice singlet is more incoherent in LSCO than in NCCO (see Fig. 3(a)).

Figure 7(b) is a blow up of Fig. 7(c), that displays the integrated spectrum on a larger energy scale. The LHB is separated from the UHB by an energy scale of the order of U_d . It is worth noting that the $p_{\pm z}$ and $d_{3z^2-r^2}$ orbitals have a strong weight between -4 and -1 eV, and the in-plane oxygens are located at -5 eV. Hence, the additional orbitals $p_{\pm z}$ and $d_{3z^2-r^2}$ hybridize with the Zhang-Rice singlet, and change the theoretical description of LSCO for energies larger than 1 eV.

The Fermi surface of LSCO is shown in Fig. 8. The results were obtained with the three-band description, in order to compare with the Fermi surface of NCCO (see Fig. 6). At small hole doping, magnetism is present, and the spectral weight is mainly located [Figs. 8(a) and 8(b)] at the nodal k

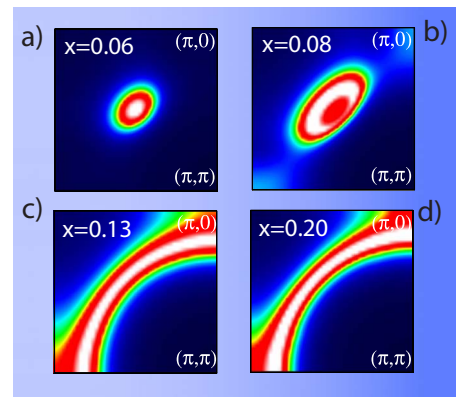


FIG. 8. (Color online) Fermi surface obtained by single-site DMFT calculations for the three-band description of LSCO in the ordered state. The Fermi surface at low doping [(a) and (b)] is centered around $M=(\pi/2, \pi/2)$, and is moving toward the Fermi arc shape [(c) and (d)] when magnetism is destroyed.

point $\mathbf{k}=(\pi/2, \pi/2)$, in agreement with experiments.⁶⁴ Upon larger doping [Figs. 8(c) and 8(d)], magnetism is destroyed and the Fermi surface has the same shape as given by LDA. Interestingly, for NCCO Fermi-liquid behavior is observed at moderate doping close to the antinodal direction, and in NCCO there is only a small weight along the nodal direction [see Figs. 6(f) and 6(g)]. For LSCO, the situation is very different, the spectral weight along the Fermi surface is quite uniform at moderate doping [see Figs. 8(c) and 8(d)]. Our Fermi-surface evolutions are also in good agreement with other theoretical approaches which can describe antiferromagnetism in correlated systems, such as DMFT+ Σ .⁶⁵

In Figs. 9(a) and 9(c) we focus on the momentum resolved spectral functions of doped LSCO. Figures 9(b) and 9(d) are the corresponding integrated spectral functions. At 10% doping [Fig. 9(b)], the ZR singlet has an incoherent contribution and a coherent part—the QP. The coherent part (QP) is the narrow band below the Fermi level in Fig. 9(a). The vertical arrows in Figs. 9(a) and 9(c) highlight the location of the direct transitions from occupied states to unoccupied states. These transitions are important for the optical conductivity (which we discuss in the next section).

For comparison, we also show the theoretical description of LSCO without the apical oxygens in Figs. 9(e) and 9(f). The main difference between the three-band and the six-band descriptions is that the incoherent part of ZR is narrower in the three-band theory. The vertical transitions, marked with vertical arrows in Figs. 9(c) and 9(e), highlight large contributions to the optical conductivity, and one can see that the optical transitions occur at different energies in the two models.

Figure 9(g) is the momentum resolved spectral function around a nodal cut of the Brillouin zone. We observe the presence of a very sharp kink in the dispersion (waterfall), in agreement with experimental data of Ref. 66 reproduced in Fig. 9(h).

Figures 10(a)–10(d) displays the orbital resolved spectral functions, obtained within a six-band theory, for various dopings on a wide energy scale. Upon doping [Figs. 10(b)–10(d)] we observe the presence of the quasiparticle

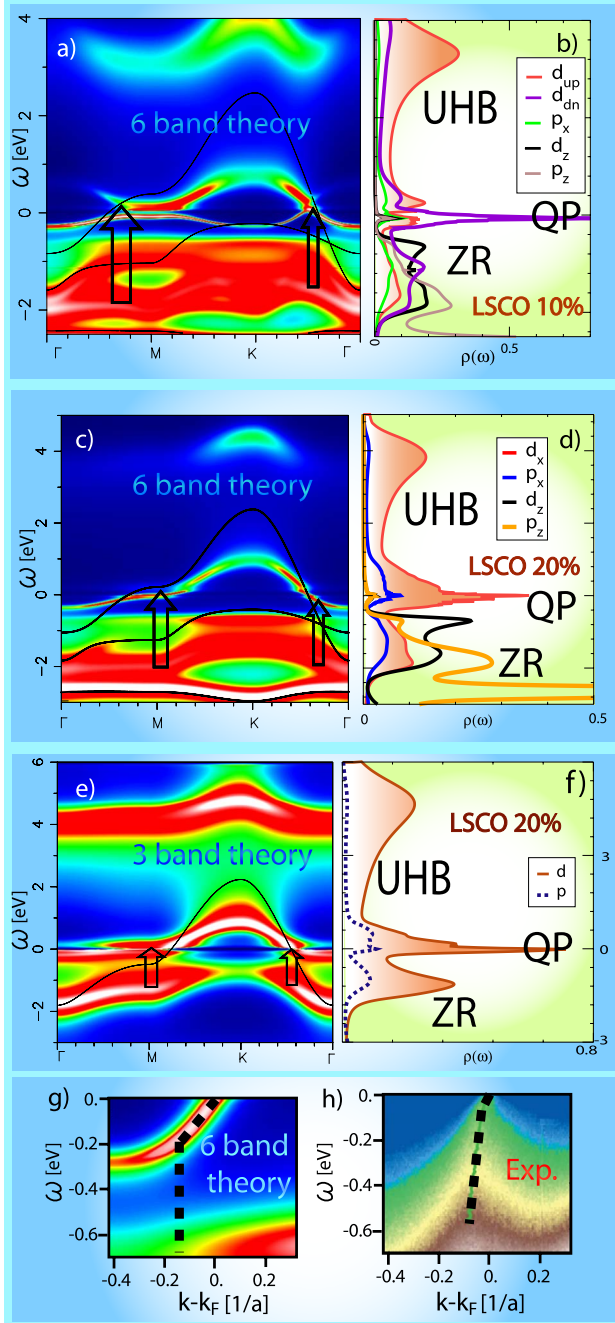


FIG. 9. (Color online) [(a) and (c)] Frequency-dependent spectral weight $A(k, \omega)$ obtained by LDA+DMFT of a six-band model description of doped LSCO. (b) and (d) Partial density of states of the $d_{x^2-y^2}$, $d_{3z^2-r^2}$, $p_{(x,y)}$, and $p_{\pm z}$ orbitals. (a) and (b) are obtained in the ordered state. (e) and (f) are obtained within a three-band description of doped LSCO and are shown for comparison. The optical transitions occur at different energies for the three-band and six-band theories (see vertical arrows in c and e). Also note that the weight of the $d_{3z^2-r^2}$ and $p_{\pm z}$ orbitals in (b) and (d) close to the Fermi level is consequent, which justifies that a six-band description is necessary. The solid lines in (a), (c), and (e) are the rigid LDA bands. (g) $A(k, \omega)$ along the nodal cut of the Brillouin zone for the paramagnetic six-band theory at 10% doping, compared side by side with (h) experimental data of Ref. 66. The dashed line are guide to the eyes to illustrate the sharp kink (waterfall) in the dispersion.

peak and the UHB smears out. Additionally, in the doped compound the $d_{3z^2-r^2}$ and $p_{\pm z}$ orbitals have a larger weight close to the Fermi level.

Figure 10(e) show the relative occupation (in hole notation) of the $d_{3z^2-r^2}$ and $p_{\pm z}$ orbitals upon doping. Our results are in agreement with Ref. 68 and we find that even after inclusion of the apical oxygens, there is no saturation of the occupancy observed around doping 0.2 in the XAS experiments of Ref. 69. We notice however that LDA+DMFT does capture the evolution of the *ratio of the occupancies* of apical and planar oxygens: for doping $\delta < 20\%$, the holes go mainly to the $d_{x^2-y^2}$ and $p_{(x,y)}$ orbitals, and for larger doping $\delta > 20\%$, the holes start to fill the $d_{3z^2-r^2}$ and $p_{\pm z}$. In Fig. 10(f) we report the experimental data of Ref. 67 for side-by-side comparison with DMFT calculations. Our calculations reproduce the rapid increase in the occupancy of p_z around doping 0.2.

We note that modeling XAS more accurately may require downfolding the LDA bands over a much larger energy range to include more orbitals, or the inclusion of the doping dependence modifications of the apical oxygen distance to the copper oxide layer pointed out in Ref. 70. A more accurate modeling of the XAS, including the core hole potential, as it was done for the core-level photoemission in Ref. 71, might also be necessary.

VI. OPTICAL PROPERTIES OF LSCO AND NCCO

We now turn to the optical conductivity. It was previously computed for the three-band model of LSCO (Ref. 31) and we now generalize the results for the six-band description of LSCO and we also compute it for NCCO (see Fig. 11).

The optical conductivity in LDA+DMFT is given by

$$\sigma'(\omega) = \frac{1}{N_k} \sum_{\sigma k} \frac{\pi e^2}{\hbar c} \int dx \frac{f(x-\omega) - f(x)}{\omega} \times \text{Tr}(\hat{\rho}_{\mathbf{k}\sigma}(x-\omega) \mathbf{v}_{\mathbf{k}} \hat{\rho}_{\mathbf{k}\sigma}(x) \mathbf{v}_{\mathbf{k}}), \quad (7)$$

where c is the interlayer distance and the density matrix $\hat{\rho}$ is defined by

$$\hat{\rho}_{\mathbf{k}\sigma}(x) = \frac{1}{2\pi i} [\mathbf{G}_{\mathbf{k}\sigma}^\dagger(x) - \mathbf{G}_{\mathbf{k}\sigma}(x)]. \quad (8)$$

The bare vertex for a multiple orbital problem $v_k^{\alpha,\beta} = \frac{dH_k^{\alpha,\beta}}{dk_x} + i(q_x^\alpha - q_x^\beta)H_k^{\alpha,\beta}$ is obtained following the steps of Ref. 75. The Peierl phase $i(q_x^\alpha - q_x^\beta)H_k^{\alpha,\beta}$ plays an important role, in particular, for the ordered state (as discussed in Ref. 75, if this phase is not considered the optical conductivity depends on any artificial folding of the Brillouin zone).

In Fig. 11(a) we show the theoretical optical conductivity of NCCO at integer filling (red curve) and at 10% doping (blue curve). The undoped compound has a sharp onset at an energy on the order of 1.5 eV which we interpret as the direct gap [slightly larger than the charge-transfer gap in Fig. 3(b)].

Doping introduces several new features [blue line in Fig. 11(a)]. The 1.5 eV optical peak disappears and the weight is transferred to lower energy in the form of a Drude peak and a mid infrared peak at $\omega \approx 0.2$ eV. The optical conductivity

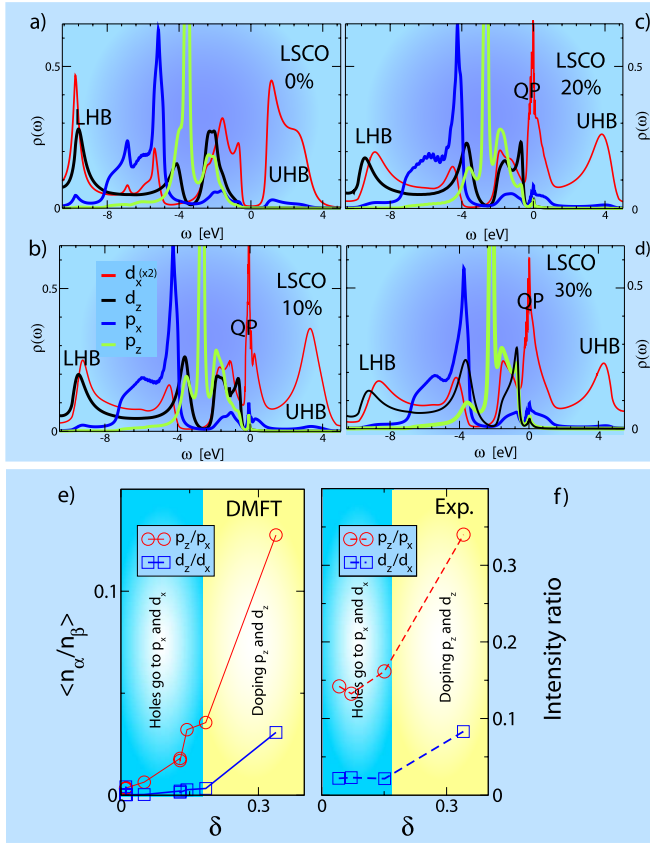


FIG. 10. (Color online) Spectral functions for the six-band theory of LSCO in (a) the parent compound and at (b) 10% and (c) 20% doping and (d) 30% doping. The $d_{x^2-y^2}$, $d_{3z^2-r^2}$, $p_{(x,y)}$, and $p_{\pm z}$ components are shown. Note that the LHB at -9 eV is both of $d_{x^2-y^2}$ and $d_{3z^2-r^2}$ character. At finite doping (b) and (c), there is a QP close to the Fermi energy. Note that the $d_{3z^2-r^2}$ and $p_{\pm z}$ weight gets closer to the Fermi level for higher doping (c). These latter orbitals will therefore be important to describe high doping and/or high energy spectroscopy. (e) Ratio of the hole occupancy of the $d_{3z^2-r^2}$ and $d_{x^2-y^2}$ orbitals (squares) and of the $p_{\pm z}$ and $p_{(x,y)}$ orbitals (circles) obtained by DMFT, and (f) experimental data are also shown for comparison (Ref. 67).

also displays a peak in the magnetic solution at a much lower frequency $\omega \approx 0.035$ eV [see left inset of Fig. 11(a)].

Below 0.5 eV, vertical transitions are among the quasiparticle bands of the magnetic DMFT band structure. This involves a continuum of k points but it is likely to be controlled by saddle points in the reciprocal space. One saddle is at $M=(\pi,0)$ and transitions close to that point, indicated by a vertical arrow in Fig. 3(c), give rise to the peak in the optical conductivity at 0.2 eV. Transitions close to the midpoint between $K=(\pi,\pi)$ and $\Gamma=(0,0)$, give rise to the small peak at 0.035 eV in the optical conductivity. Both peaks are characteristics of the quasiparticle band structure in the magnetic state of NCCO, and these features are not present in the absence of magnetic order, as shown in Fig. 12(a). The absence of the peak at 0.035 and 0.2 eV in the optical conductivity is explained by the absence of vertical transition in the k -dependent spectral weight $A(k,\omega)$ [see Fig. 12(b)], which are present in the ordered state and highlighted by the vertical arrow of Fig. 3(c).

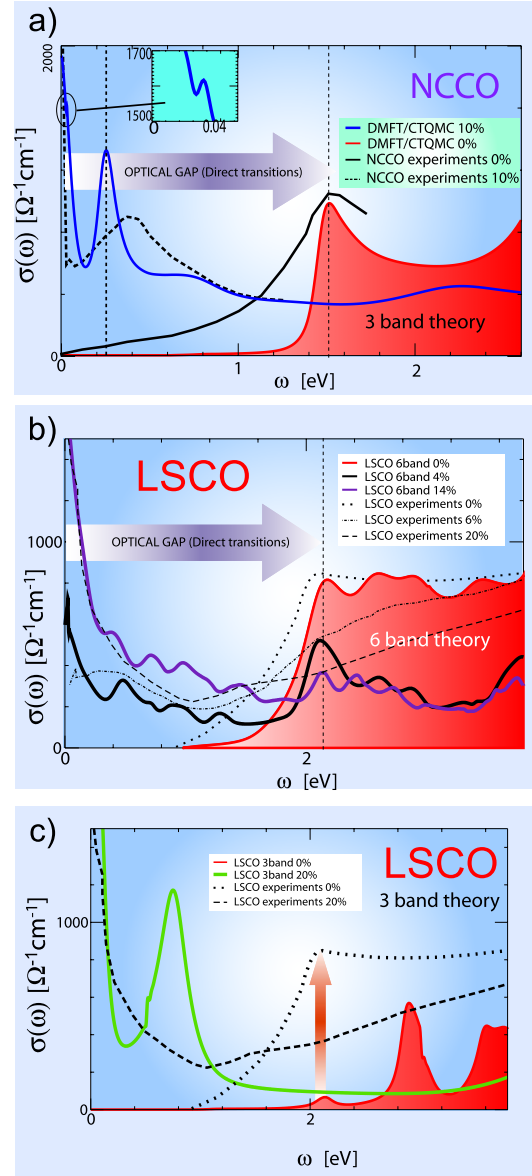


FIG. 11. (Color online) (a) Theoretical optical conductivity of NCCO in $\Omega^{-1}\text{cm}^{-1}$ at integer filling (red line). We find that NCCO has an optical gap of about 1.5 eV, which is larger than the direct gap ≈ 1.2 eV. We also show data for doped NCCO (blue line). Note that for doping smaller than 20%, we observe a small peak at a small energy ≈ 0.035 eV (see the inset). We also observe a second peak at larger energy scale ≈ 0.2 eV, which corresponds to optical transitions within the Zhang-Rice singlet [see Fig. 3(c)]. For comparison we also show the infrared optics of Refs. 72 and 73 (dashed black line). (b) Optical conductivity of the six-band theory of LSCO for the parent compound (red line) and doped LSCO. For comparison we also show experimental data of Ref. 74 (short and long-dashed lines). (c) Optical conductivity of the three-band theory of LSCO in the parent compound (red line) and doped LSCO (yellow line), and experimental data of Ref. 74 (short and long-dashed lines). The vertical arrow in panel (c) emphasizes the disagreement between theory and experiments. Note also that at finite doping there is a peak at 0.8 eV in the optical conductivity of the three-band theory, which is absent from experimental data. This peak is related to the optical transitions shown in Fig. 9(e) (see the vertical arrows). All calculations were done in the ordered state.

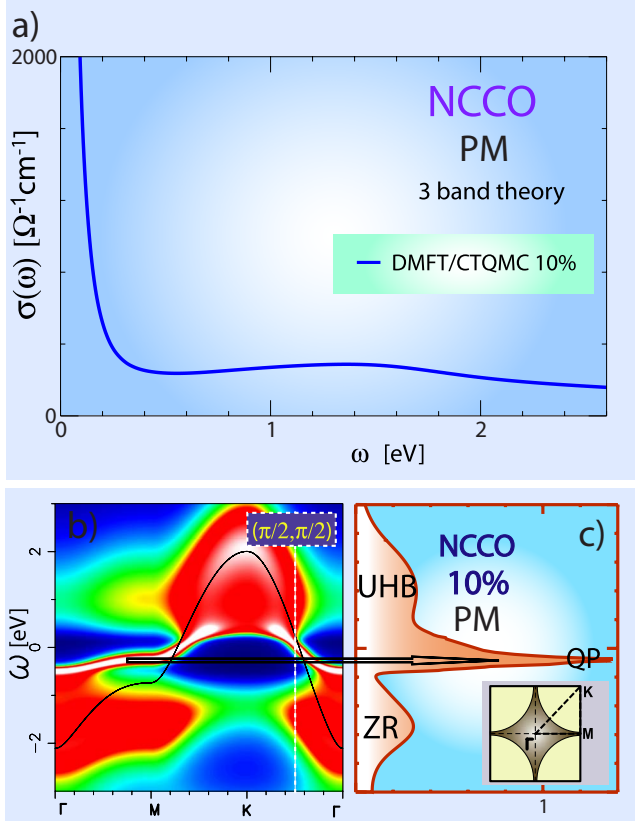


FIG. 12. (Color online) (a) Theoretical optical conductivity of paramagnetic NCCO at 10% doping is shown. In the paramagnetic state of NCCO, there are no peaks at 0.035 and 0.2 eV which are observed in the magnetic state of NCCO at same doping [see Fig. 11(a)]. (b) We show the k -dependent spectral weight $A(k, \omega)$ for NCCO at 10% doping. (c) We show the corresponding total density of states. In the paramagnetic state of NCCO there is no splitting of the quasiparticle peak QP [see Fig. 3(d)].

The quasiparticle peak in the ordered state is split into two narrow bands, one above and one below the Fermi level [see Fig. 3(d)] while the splitting is absent in the paramagnetic state [see Fig. 12(c)]. This is due to the absence of the pseudogap around $(\pi/2, \pi/2)$ in the paramagnetic state [see Fig. 12(b)]. As a consequence, the paramagnetic Drude peak is featureless while in the ordered state we observe several low-energy peaks in the optical conductivity (at 0.035 and 0.2 eV).

The agreement between DMFT and experimental data^{72,73} [dashed line of Fig. 11(a)] is qualitative and our theory connects the peak in the experimental optical conductivity at 0.4 eV with magnetism, in agreement with Ref. 76. Additionally our study allow us to connect this peak with the spectral weight below the Fermi energy at the $M=(\pi, 0)$ point, which is present in both the paramagnetic and the ordered states.

We note finally that the peak in the optical conductivity at smaller energy 0.035 eV is observed at this energy in experiments (see Fig. 2 of Ref. 77), which is only present within the ordered state and disappears at higher temperature in the paramagnet, which suggest that this feature is not connected to phonons. Our calculation connects this peak to the presence of magnetism and to the pseudogap around $(\pi/2, \pi/2)$ [see Fig. 3(c)].

We now turn to the description of the optical conductivity of LSCO. In Fig. 11(b) we show the optical conductivity of the six-band description of LSCO in the parent compound (red curve) at 4% (black curve) and 16% doping (blue curve). For comparison we also show experimental data of Ref. 74 at 0% doping (dotted line), 6% (short dashed), and 20% (long dashed). Note that there is a quantitative agreement between the theory and experiments for frequencies smaller $\omega < 2$ eV. At larger frequencies $\omega > 2$ eV, the optical conductivity in experiments is larger than the theoretical one, which is due to optical transition from additional orbitals that are not present within our calculations, and which contributes at high energies.

For comparison, we now also consider the three-band theory of LSCO. In Fig. 11(c) we show the optical conductivity of the magnetic state of the parent compound (red curve) and of the doped LSCO at 20% doping (yellow curve). We also show the experimental data of Ref. 74 at 0% doping (dotted line) and 20% doping (dashed line). The vertical arrow emphasizes the disagreement between theory and experiments. The strong differences between the three-band and six-band calculations for the optical conductivity of the parent compound is related to the strong weight of the $p_{\pm z}$ and $d_{3z^2-r^2}$ orbitals below the Fermi level, which are mainly occupied and contribute significantly to the optical conductivity. This weight is obviously absent in the three-band theory. Note also that at finite doping there is a peak at 0.8 eV in the optical conductivity of the three-band theory, which is absent in experimental data. This peak is related to the optical transitions shown in Fig. 9(e) by the vertical arrows. This artifact of the three-band calculations is cured by introducing the $d_{3z^2-r^2}$ and $p_{\pm z}$ orbitals.

To quantify the rate of the redistribution of optical spectral weight, we computed the effective electron number per Cu atom defined by

$$N_{eff}^{\Lambda} = \frac{2m_e V}{\hbar \pi e^2} \int_0^{\Lambda} \sigma'(\omega) d\omega, \quad (9)$$

where m_e is the free-electron mass and V is the cell volume containing 1 f.u. N_{eff} is proportional to the number of electrons involved in the optical excitations up to the cutoff Λ .

Our results for N_{eff} are displayed in Fig. 13 and compared to experimental data taken from Refs. 74, 78, and 79. Notice a favorable agreement between the theory and experiment, for which the use of the realistic electronic structure is essential. Moreover, we also show in Fig. 13 the static mean-field results. We emphasize that the static mean field is not able to reproduce qualitatively the experimental trend. This highlights the importance of the dynamical fluctuations not taken into account in Hartree-Fock. The trend of N_{eff} is qualitatively similar for both LSCO and NCCO, and therefore does not show that LSCO and NCCO are qualitatively different: the former being a Mott and the latter being a Slater insulator.

We also compute the temperature dependence of N_{eff} for NCCO and LSCO at a fixed density. In Fig. 14(a) we show the theoretical results for NCCO. We plot in the same figure the temperature dependence of N_{eff} (left scale) and the tem-

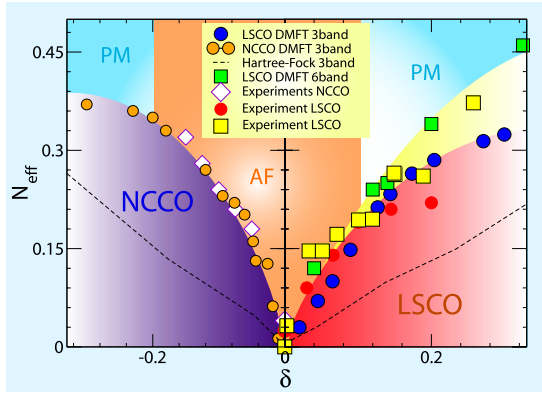


FIG. 13. (Color online) We show the dimensionless integrated optical conductivity N_{eff} for the three-band study of LDA+DMFT done on LSCO (Ref. 31) and NCCO, obtained with a cutoff $\Lambda=1.2(\Lambda=1.5)$ for NCCO (LSCO). Experimental data for LSCO [red circles (Ref. 74) and yellow squares (Ref. 78)] and NCCO (Ref. 79) (open diamonds) are shown. The increase in N_{eff} is similar for both compounds. The dashed line indicates the results obtained by the Hartree-Fock approximation. We also show for comparison results obtained within the six-band theory (green squares). The agreement between theory and experiments is quantitative.

perature dependence of the magnetic moment (right scale). We find that N_{eff} is reaching a maximum value when the magnetization is suppressed by thermal fluctuations at ≈ 400 K. There is actually a variation in N_{eff} inside the ordered phase that can be explained by the destruction of the magnetic pseudogap. Once the magnetization is quenched by the temperature, heating the system further reduces N_{eff} . The qualitative agreement with experimental data extracted from Ref. 79 is very encouraging.

The temperature dependence of N_{eff} for LSCO is shown in Fig. 14(b). We emphasize that the temperature dependence of N_{eff} shows an opposite trend for LSCO. When doping the parent compound, there is a *decrease* in N_{eff} in LSCO, whereas there is an *increase* in N_{eff} in NCCO. Therefore the temperature dependence of N_{eff} clearly shows a distinct behavior for a Slater and a Mott insulator. Note that the same general trend of the temperature dependence of N_{eff} is observed in experiments for LSCO but for a larger doping than the one considered here (optical data for 13% doping in Fig. 6 of Ref. 80).

The trend of N_{eff} can be understood in a simple picture. In a Slater picture, the onset of antiferromagnetism reduces the Coulomb correlations (double occupancy) at the expense of the kinetic energy. The opposite is true in a charge-transfer insulator. Consequently, in a Slater insulator the kinetic energy becomes less negative as the temperature decreases while the opposite happens in a charge-transfer insulator. The kinetic energy as a function of temperature is readily available in the theory and is displayed in Figs. 15(a) and 15(c) and the Coulomb energy is displayed in Figs. 15(b) and 15(d).

In Fig. 15(f) we display the imaginary part of the self-energy at zero frequency, $\text{Im} \Sigma(\omega=0)$, as a function of the temperature, which is proportional to the scattering rate $\lambda = -\text{Im} \Sigma(\omega=0)$. We find that the scattering rate of LSCO is

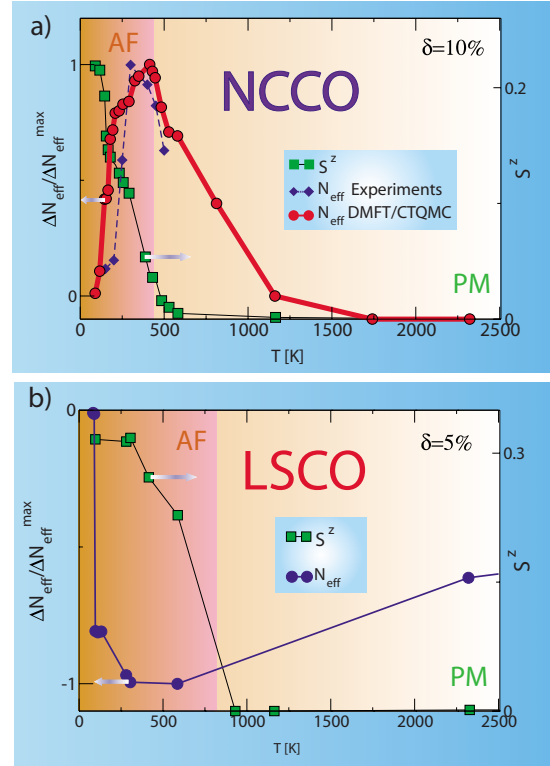


FIG. 14. (Color online) (a) Three-band theoretical normalized variation in N_{eff} , $\Delta N_{eff} = N_{eff}(T) - N_{eff}(T=89 \text{ K})$, at 10% electron doping for NCCO (red circles, left scale). N_{eff} is reaching a maximum value when the magnetization (orange squares, right scale) is destroyed by the thermal fluctuations. The decrease in N_{eff} at low temperature can be explained by the opening of a pseudogap in the ordered phase. The data were obtained by single-site DMFT calculations in the ordered phase. The dashed line corresponds to experiments [see Fig. 7c of Ref. 79], where they measured $N_{eff}(\Lambda=0.03 \text{ eV})$ (contribution due to the Drude peak) and $N_{eff}(\Lambda=0.3 \text{ eV}) - N_{eff}(\Lambda=0.2 \text{ eV})$ (contribution due to the pseudogap). The dashed line corresponds to the sum of these two contributions. (b) Three-band single-site DMFT of the ordered phase of LSCO is shown for 5% doping. Note that the trend of N_{eff} is opposite between LSCO AND NCCO, which is a signature that NCCO is a Slater insulator and LSCO a Mott insulator.

strongly reduced for $T < T_{Neel}$ (T_{Neel} is highlighted by the red vertical arrow), which is consistent with the kinetic-energy reduction observed for LSCO at low temperature [see Fig. 15(c)]. The scattering rate of NCCO is much smaller and is only weakly temperature dependent, which is a consequence of NCCO being less correlated than LSCO.

Hence the location of NCCO and LSCO, relative to the metal-to-charge-transfer-insulator boundary,¹¹ accounts for the observed trends in the temperature dependence of the optical conductivity. Similar trends of temperature dependence of the kinetic energy for both electron- and hole-doped cuprates were reported in Ref. 81.

Figure 16(a) displays the kinetic-energy difference between the paramagnet and the ordered states, as a function of doping at a fixed temperature $T=89$ K, for NCCO and LSCO. The difference of Coulomb energy is shown in Fig. 16(b). We find that in NCCO, the ordered phase is stabilized

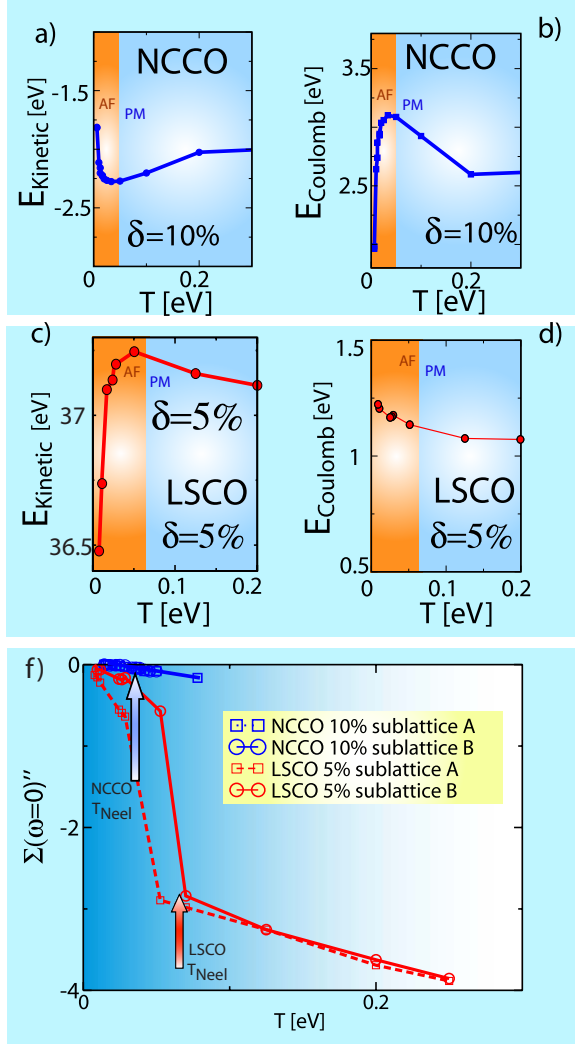


FIG. 15. (Color online) Three-band theoretical temperature dependence of the (a) kinetic energy \mathcal{H}_t [Eq. (1)] and (b) Coulomb energy \mathcal{H}_U [Eq. (2)] of NCCO at 10% doping, and (c) Kinetic and (d) Coulomb energy of LSCO at 5% doping. The red area highlights the temperature region where the solution is magnetic (AF), and the solution is PM in the blue area. (a) and (b) are showing that there is a kinetic-energy optimization when LSCO becomes an antiferromagnet, which is proper to the Mott insulator, and (c) and (d) show that NCCO is a typical Slater insulator, which optimizes the Coulomb (local on-site repulsion) energy when it becomes an antiferromagnet, at the expense of a worse kinetic energy. This is consistent with the theoretical N_{eff} shown in Fig. 14(f). We show the imaginary part of the self-energy at zero frequency $\text{Im} \Sigma(\omega=0)''$ in function of the temperature. The scattering rate of LSCO $\lambda = -\text{Im} \Sigma(\omega=0)$ (red lines) is strongly reduced for $T < T_{Neel}$ (T_{Neel} is highlighted by the red vertical arrow), which is consistent with the kinetic-energy reduction observed for LSCO at low temperature [Fig. 15(c)]. NCCO (blue lines) is showing a small scattering rate weakly dependent on the temperature, which is consistent with NCCO being more metallic than LSCO. All calculations were obtained by CTQMC in the ordered state.

by optimizing the on-site repulsion (Coulomb energy) at a cost in the kinetic energy. This is typical for a Slater insulator and is also captured by a simple Hartree-Fock static mean-

field theory. In LSCO the trend is opposite, the ordered phase is stabilized by having a lower kinetic energy, at a cost in the Coulomb energy.

Very interestingly, in a one-band theory an increase in the order parameter $\langle S^z \rangle$ leads necessary to a decrease in the Coulomb energy,⁸²

$$\langle (S^z)^2 \rangle = \frac{1}{4} \langle (n_\uparrow - n_\downarrow)^2 \rangle = \frac{1}{4} (n - 2\langle n_\uparrow n_\downarrow \rangle) \quad (10)$$

and therefore

$$\langle n_\uparrow n_\downarrow \rangle = \frac{n}{2} - 2\langle (S^z)^2 \rangle. \quad (11)$$

In the ordered phase there is hence an increase in $(S^z)^2$ and a decrease in $\langle n_\uparrow n_\downarrow \rangle$ for a fixed density n or doping δ .

In a three-band theory this is not the case since the density n in formula (11) is not the total density but the density of the d orbital n_d . The latter quantity is not fixed at a given doping and is hence increased when the magnetization is increased. For the parent compound of LSCO, we found that magnetic correlations lead to an increase in n_d of 1.4% and to an increase in the double occupancy $n_{d\uparrow} n_{d\downarrow}$ of 6%. Hence our results highlight a significant difference between the single-band and three-band theoretical descriptions of LSCO and NCCO.

VII. STRENGTH OF CORRELATIONS IN LSCO AND NCCO

We finally extended the three-band calculations to other values of $\epsilon_d - \epsilon_p$, in order to study the dependence of our results on the charge-transfer energy $\epsilon_d - \epsilon_p$. We emphasize that the charge-transfer energy plays the role of an effective repulsion U in the one-band model language, and hence controls the strength of the correlations in a three-band theory. For instance, it was shown in the seminal ZSA paper¹¹ that if the Coulomb repulsion of the d orbital is larger than the charge-transfer energy $\epsilon_d - \epsilon_p$, the size of the gap in the paramagnet is independent of the Coulomb repulsion, and the strength of correlations is set by the charge-transfer energy.

In order to study the strength of the correlations, we computed the jump in the chemical potential $\delta\mu$ for infinitesimal doping of the parent compound. This quantity gives an estimation for the gap in the spectral functions of the parent compound, which is around 1.2 eV and 1.8 eV in NCCO and LSCO, respectively. We present the data for both the ordered state and the paramagnetic state of LSCO and NCCO in Figs. 17(a) and 18(a), respectively. The jump of chemical potential in the paramagnet gives an estimation of the critical charge-transfer energy Δ_{c2} , which is the maximum charge-transfer energy that allows the metallic solution. However at Δ_{c2} the ordered solution has a substantial gap, which is closely related to $\delta\mu$ in the ordered state. We find that $\delta\mu$ in the ordered state of NCCO is around 1.2 and 1.8 eV in LSCO. Hence, we conclude that NCCO [Fig. 17(a)] is slightly below the charge-transfer-insulator-to-metal transition Δ_{c2} . Indeed, below Δ_{c2} , the magnetic long-range correlations are necessary to open a gap and slightly above Δ_{c2} the paramagnetic

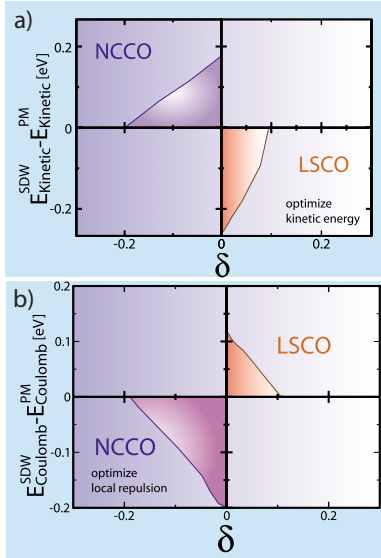


FIG. 16. (Color online) Three-band theoretical energy differences between the antiferromagnetic and the paramagnetic phases. We show the doping dependence of the (a) kinetic energy \mathcal{H}_t [Eq. (1)] and (b) Coulomb energy \mathcal{H}_U [Eq. (2)] of NCCO and LSCO at fixed temperature $T=89$ K. There is a kinetic-energy optimization when LSCO becomes an antiferromagnet, which is proper to the Mott insulator, and NCCO is a typical Slater insulator, which optimizes the Coulomb (local on-site repulsion) energy when it becomes an antiferromagnet, at the expense of a worse kinetic energy. This is consistent with the temperature dependence of the theoretical N_{eff} shown in Fig. 14 and with the temperature dependence of the kinetic and Coulomb energies 15. All calculations were obtained by CTQMC.

gap is much smaller than the Slater gap induced by the nesting, as shown in Fig. 17(a).

The two solutions of the DMFT equations for NCCO are shown in panels, Figs. 17(b) and 17(c). The first one is nonmagnetic and metallic, and describes a material in the absence of long-range order. The second is insulating and antiferromagnetically ordered, with a charge-transfer gap of 1.2 eV. Since the nonmagnetic solution is metallic, the magnetic long-range order is responsible for the insulating nature of NCCO (Slater insulator).

We find that LSCO [Fig. 18(a)] is above Δ_{c2} , as reported in a recent study.³¹ Indeed, the parent compound of LSCO is only weakly affected by the presence of magnetic order, the size of the gap is only slightly increased when magnetic order is present. The DMFT equations for LSCO have two solutions, shown in panels, Figs. 18(b) and 18(c). The first one is paramagnetic and the second is antiferromagnetically ordered, with a charge-transfer gap of 1.8 eV. Since the paramagnetic solution is insulating, the magnetic long-range order is not responsible for the insulating nature of LSCO (Mott insulator).

In Figs. 19(a)–19(c), we show the density of states of the three-band description of the parent compound of LSCO using various numerical tools. In panel (a) we show the density of states obtained by ED for the paramagnet and the ordered states. In panel (b) we show the density of states obtained by CTQMC and in panel (c) the density of states obtained by a

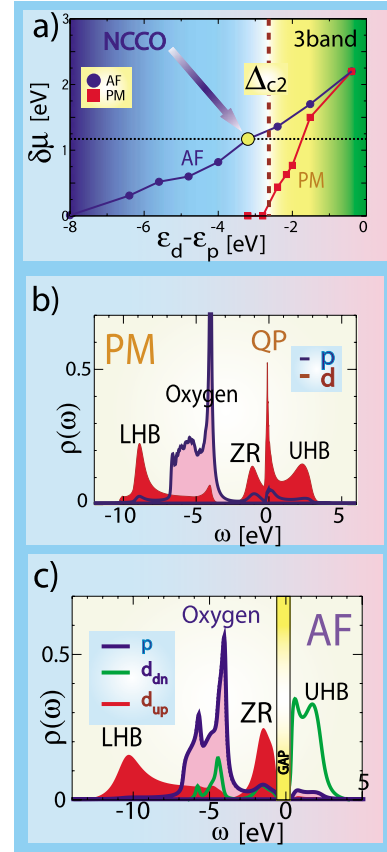


FIG. 17. (Color online) (a) We show the jump in the chemical potential $\delta\mu$ in the ordered state of NCCO (blue circles) for other values of the charge-transfer energy $\epsilon_d - \epsilon_p$. The results are obtained for the three-band single-site DMFT. For comparison, we also show the jump in the chemical potential of the paramagnet (red squares). There is a quantum critical point Δ_{c2} for the paramagnetic state, with respect to the charge-transfer energy, corresponding to the metal to charge-transfer insulator transition. The physical value obtained by LDA+DMFT for $\epsilon_d - \epsilon_p$ places NCCO below the boundary. (b) Density of states of the paramagnetic state of NCCO. The quasiparticle peak close to the Fermi energy (QP) is a signature that NCCO is paramagnetic metal. (c) Density of states of the ordered state of NCCO.

recent DMRG solver.⁵⁰ We conclude that the gap in the ordered state of LSCO is of similar size than the gap obtained in the paramagnet, independently of the numerical solver used to solve the DMFT equations. In Fig. 19(d) we show the doping as a function of the chemical potential, and it displays a plateau related to the charge gap at integer filling. The agreement between the different solvers gives us confidence in these results.

The asymmetry between both NCCO and LSCO, being below and above the charge-transfer-insulator-to-metal transition Δ_{c2} , is a simple explanation for the striking asymmetry in their phase diagram. For LSCO, the magnetic correlations are destroyed rapidly upon doping while in the NCCO they survive up to high doping, as shown in Fig. 1(a).

In this section, we emphasized that the physical origin of the asymmetry between LSCO and NCCO lies not only in the different values of the oxygen-oxygen overlap, which

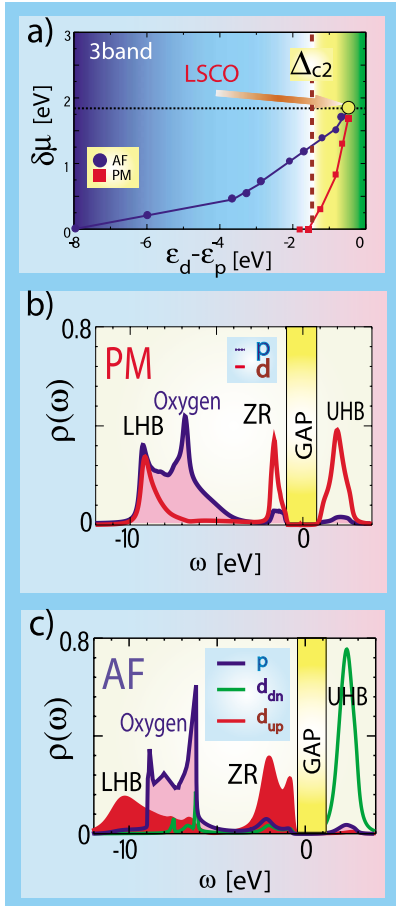


FIG. 18. (Color online) (a) We show the jump in the chemical potential $\delta\mu$ in the ordered state of LSCO (blue circles) for other values of charge-transfer energy $\epsilon_d - \epsilon_p$. The results are obtained for the three-band single-site DMFT. For comparison, we also show the jump in the chemical potential of the paramagnet (red squares). There is a quantum critical point Δ_{c2} for the paramagnetic state, with respect to the charge-transfer energy, corresponding to the metal to charge-transfer insulator transition. The physical value obtained by LDA+DMFT for $\epsilon_d - \epsilon_p$ place LSCO above the boundary. (b) Density of states of the paramagnetic state of LSCO, which shows the presence of a gap. This is a signature that LSCO is a Mott insulator (c) density of states of the ordered state of LSCO. The gap in the density of states is of similar size for the paramagnetic insulator and the ordered state as shown in details in Fig. 19.

controls the curvature of the Fermi surface, an effect that is captured in model Hamiltonian studies, but also in the different values of the charge-transfer gap in the two structures. The latter has an electrostatic origin, the electron-doped material lacks the negatively charged apical oxygen, which increase the electrostatic potential at the copper site.

For comparison, we now also discuss results of the one-band Hubbard model. In Fig. 20 we show the gap in the density of states for the paramagnetic insulator and for the antiferromagnetic insulator. In the one band model exists a critical point U_{c2} which separates the paramagnetic metal at small U/t from the paramagnetic insulator at large U/t (squares). The magnetic solution is always insulating (circles). Using typical values for the hopping parameter t

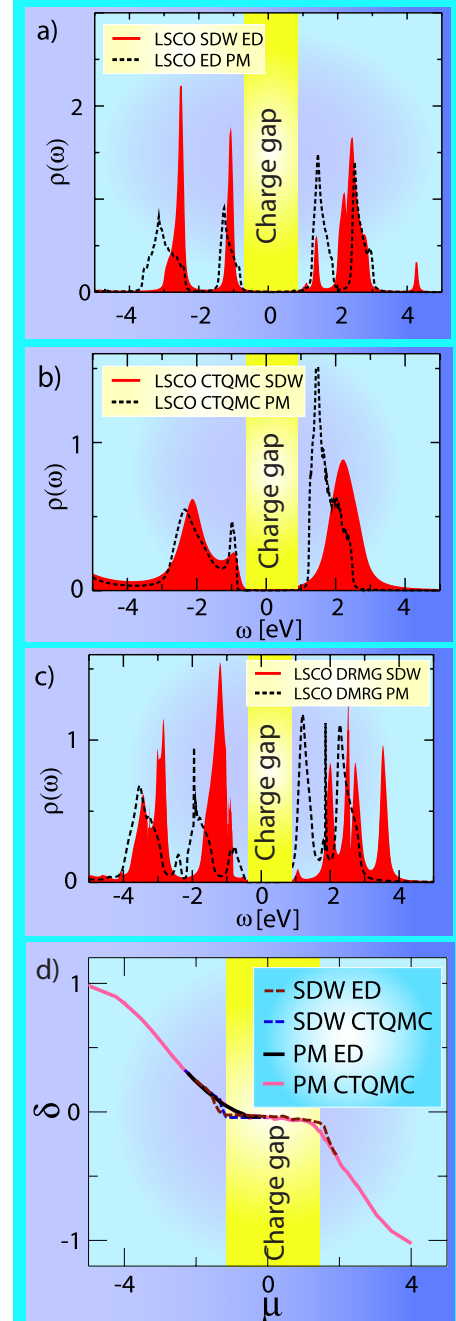


FIG. 19. (Color online) Density of states of the three-band description of the parent compound of LSCO in the paramagnetic (dashed line) and ordered state (red area) obtained with different solvers: (a) ED, (b) CTQMC, and (c) DMRG. All data show that LSCO is a paramagnetic insulator, and that the size of the gap obtained by the density of states is similar for both the paramagnet and the ordered state (within $\approx 10\%$). (d) We show the variation in the doping δ with respect to the chemical potential μ for both the ordered state (spin-density wave) and the PM state obtained by ED and CTQMC. There is a jump in the chemical potential $\delta\mu$ (plateau at $\delta=0$) of similar size for all data. This shows that the magnetic correlations do not strongly affect the insulating properties of LSCO.

(Ref. 83) ($t=0.42$ eV for NCCO and $t=0.43$ eV for LSCO), and typical values for the gap Δ in the ordered state for

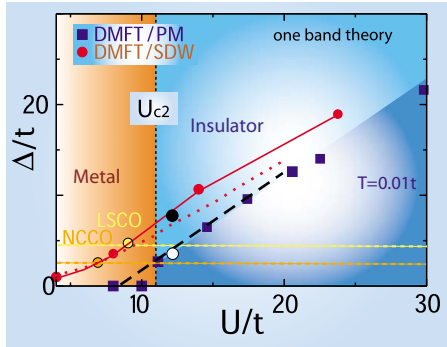


FIG. 20. (Color online) We show calculations done on the one-band Hubbard model for various Coulomb repulsion U and transfer integral t ratios. In the one-band theory there is also a quantum critical point U_{c2} that is the minimal repulsion driving a paramagnet to an insulator. Locating the compounds LSCO and NCCO by fitting the gap Δ [$\Delta=1.2$ eV and $t=0.42$ eV (Ref. 83) for NCCO and $\Delta=1.8$ eV and $t=0.43$ eV for LSCO], we place both LSCO and NCCO below U_{c2} in the one band picture. It is worth noting that for large enough U/t the size of the paramagnetic gap is close to the gap in the ordered state. Results were obtained by using single-site DMFT with exact diagonalization. For comparison we show theoretical calculations of Ref. 37, done for the paramagnet (long-dashed line) and the ordered state (short dotted line), and the theoretical calculations of Ref. 36 in the paramagnetic state (white circle) and in the ordered state (black circle).

LSCO and NCCO ($\Delta=1.2$ eV for NCCO and $\Delta=1.8$ eV for LSCO) we can locate the compounds in the one-band model phase diagram. Both LSCO and NCCO are below U_{c2} in this picture, in agreement with Ref. 30. There is therefore a strong difference in the physical conclusions obtained by the one-band calculations and the LDA+DMFT.

VIII. CONCLUSION

In conclusion, we carried out a comparative study of NCCO and LSCO using a realistic LDA+DMFT approach. The LDA+DMFT studies achieved overall good agreement with optical conductivity and ARPES studies in a broad range of dopings and a wide range of energy scales up to energies on the order of the charge-transfer energy.

In particular, for NCCO we found that static mean-field theory is not sufficient to describe many qualitative features due to the presence of multiple peaks in the electronic spectra. The description of these features require more sophisticated methods and studies along those lines were carried out for NCCO in Refs. 39 and 84. We demonstrated that LDA+DMFT successfully describes these effects in NCCO.

While single-site DMFT is already a good methodology to describe the phase diagram of NCCO, cluster corrections are important in the underdoped region of LSCO. This indicates the importance of singlet formation or the possible importance of other ordered states in this region. However, our LDA+DMFT gave a remarkable agreement with experiments for the optical conductivity, for doping smaller than 20% and energy scale $\omega < 2$ eV, when the $d_{3z^2-r^2}$ and $p_{\pm z}$ are considered. For larger doping and higher frequencies,

additional bands should be considered for a proper description of the photoemission spectra.

Moreover, in agreement with Ref. 68 we found that even after inclusion of the apical oxygens, single-site DMFT does not capture the saturation of the occupancy observed around doping 0.2 in the XAS experiments of Ref. 69. We notice however that LDA+DMFT does capture the evolution of the ratio of the occupancies of apical and planar oxygens, including a rapid increase in the occupancy of p_z around doping 0.2. We note that modeling XAS more accurately may require: (i) taking into account additional LDA bands and more orbitals, (ii) to include the doping dependence of the apical oxygen position pointed out in Ref. 70, (iii) nonlocal correlations beyond DMFT might be relevant as suggested in Refs. 68 and 85–87, and (iv) to include the core hole potential, as it was done for the core-level photoemission in Ref. 71, might also be necessary.

We achieved a successful description of many normal-state physical properties (optical conductivity, ARPES, and stability of magnetism) of these two archetypal cuprates. The overall quantitative agreement between LDA+DMFT and experiments, for both LSCO and NCCO gives us increased confidence in LDA+DMFT as an approach to strongly correlated materials.

We emphasize that it did not require the introduction of *ad hoc* parameters, such as a doping-dependent interaction strength. The sensitivity of the results on the choice of the charge-transfer energy, which essentially determines the strength of the correlations, was explored. We emphasize that the charge-transfer energy for NCCO and LSCO is obtained from *ab initio* calculations, and for the values obtained by first-principles calculations we obtained good agreement with experiments.

It is remarkable to obtain good quantitative agreement between theory and experiment, on energy scales on the order the charge-transfer energy. For example, our methodology gives a good agreement with experiments for the integrated spectral weight of the optical conductivity with a cutoff above the charge-transfer gap in LSCO. For this quantitative agreement it is essential to use a multiband model including the apical oxygen orbitals. The fact that these are absent in NCCO accounts for the good agreement with the magnitude of the optical conductivity obtained for this material in our earlier publication.³²

Moreover, our methodology applied to two different materials captures not only their similarities, as, for example, the doping dependence of the integrated spectral weight, but also their differences, as the doping dependence of the magnetic moment. These differences stems from their different electronic structure and is well captured by LDA+DMFT. Differences between the electron- and hole-doped cuprates have been noticed by many authors. They were interpreted as arising from both the bare hopping integrals in the one-band model Hamiltonian and the Coulomb interaction U in the Hubbard model.

However, LDA+DMFT and multiband theories are also able to capture a more fundamental difference resulting from the different strength of the correlations in these two materials, which is driven by the charge-transfer energy. Using our methodology, we determined the relative strength of the cor-

relations of LSCO and NCCO. LSCO was found to be on the insulating side of the ZSA phase boundary confirming the preliminary conclusions of Ref. 31 but in disagreement with Ref. 30 which classifies all the parent compound of the copper oxides as Slater insulators. The electron-doped compound NCCO was found to be on the metallic side of the ZSA phase boundary³² in agreement with Ref. 30 but in disagreement with Ref. 46. Indeed, the lack of apical oxygens in NCCO reduces the charge-transfer energy relative to LSCO, placing these two materials on two different sides of the ZSA phase boundary.

This work is complementary to our earlier work,³² placing the copper oxides in a region of intermediate correlation strength. For materials in this region of parameters, we found that the location of the material relative to the ZSA boundary has important physical consequences. For example, the evolutions of the optical properties with doping and temperature in NCCO and LSCO are different, in agreement with the earlier work of Ref. 81. Our results allowed to shed some light on the differences observed in LSCO and NCCO, and these differences are attributed to the location of LSCO and NCCO on the two different sides of the ZSA boundary.

This has direct consequences on physical observables at finite doping. For instance, antiferromagnetism in the Slater limit is accompanied by an increase in the expectation value of the kinetic energy (with a concomitant reduction in the double occupation) while in the Mott limit the insulating state has an optimization of the kinetic energy which is a manifestation of the increase in the expectation value of the superexchange interaction. This is a transparent interpretation of the different trends in the evolution of the optical spectroscopy in NCCO and LSCO materials.

Our method captures both the similarities and the many essential differences between the two compounds, which can be traced to their structure and atomic constituents, and, in particular, to the absence of apical oxygens in the T' structure of NCCO. However, there are still avenues to improve the single-site DMFT description of copper oxide materials, by including the effects of the nearest-neighbor Coulomb interaction between copper and oxygen and among the oxygens beyond the Hartree approximation, and inclusion of frequency-dependent screening. Many local or frequency integrated quantities are already well described by single-site DMFT but in the region of hole doping where the discrepancy between single-site DMFT and cluster DMFT is noticeable, the latter should be used to refine the description of low-energy physical properties. Finally, the fact that NCCO is below the critical value of the metal-to-charge-transfer insulator transition, is fully consistent with the observations of metallic behavior NCCO samples where all the apical oxygens are fully removed.⁸⁸⁻⁹⁰

An important direction, to be pursued is the study of other ordered states, that exist as stable or metastable solutions of the realistic single-site or cluster LDA+DMFT equations. Exploration of this landscape of DMFT solutions is a challenging project and is worthwhile to pursue in conjunction with studies of the superconducting phase. These problems are currently under investigation.

ACKNOWLEDGMENTS

We thank A.M. Tremblay, D. Basov, D. G. Hawthorn, and

G. A. Sawatzky for discussions and sharing their insights and experimental data. Numerous discussions with A. Georges, A. Amaricci, J. C. Domenge, and A. Millis are gratefully acknowledged. Adriano Amaricci shared his density-matrix renormalization-group code and Jean-Christophe Dommene shared his exact diagonalization code. K.H was supported by NSF under Grant No. NFS DMR-0746395 and Alfred P. Sloan fellowship. G.K. was supported by NSF under Grant No. DMR-0906943, and C.W. was supported by the Swiss National Foundation for Science (SNFS).

APPENDIX A

In this appendix, we discuss how the spectral weight obtained in the ordered state, $A^\alpha(\mathbf{K}, \omega)$ is mapped to the unfolded Brillouin zone for comparison with experiments. For the calculations done in the ordered state, $[A^\alpha(\mathbf{K}, \omega)]^{ij}$ is obtained in the folded Brillouin zone, and therefore is now labeled by two additional indices i, j , that are running indices over the paramagnetic unit-cell block of the extended unit cell.

The corresponding spectral weight can be obtained in the unfolded Brillouin zone by the relation,

$$A(\mathbf{k}, \omega)^\alpha = \sum_{i,j=1}^{N_{cell}} e^{ik(\mathbf{R}_i - \mathbf{R}_j)} [A^\alpha(\mathbf{K}, \omega)]^{ij}, \quad (\text{A1})$$

where N_{cell} is the number of paramagnetic unit cell contained in the extended ordered state unit cell, and $\mathbf{R}_{i,j}$ is the position of the block within the extended unit cell.

The relation between k (unfolded Brillouin zone, paramagnetic state) and K (folded Brillouin zone, ordered state) is given by

$$\mathbf{k} = (K_x A_1 + K_y B_1) \mathbf{g}_1 + (K_x A_2 + K_y B_2) \mathbf{g}_2.$$

With the following definitions. $\mathbf{K} = K_x \mathbf{G}_1 + K_y \mathbf{G}_2$, where $G_{1,2}$ are the reciprocal basis vector of the ordered state, $\mathbf{a} = A_1 \mathbf{E}_1 + B_1 \mathbf{E}_2$ and $\mathbf{b} = A_2 \mathbf{E}_1 + B_2 \mathbf{E}_2$, where \mathbf{a} and \mathbf{b} are the direct-space basis vector of the paramagnetic unit cell, and $\mathbf{E}_{1,2}$ are the direct-space basis vector of the extended state unit cell (ordered state).

APPENDIX B

In this section we show the realistic set of tight-binding parameters obtained by downfolding the LDA band structure (see Tables II and III).

TABLE II. Three-band model Hamiltonian parameters obtained by LDA downfolding for LSCO. The vector connecting the two different unit cells is shown, and the two orbitals connected by the hopping as well.

Orbitals	Vector	Amplitude
d_x-d_x	(-2, 0)	-0.01
p_y-p_y	(-2, 0)	0.010
d_x-p_x	(-1, -1)	-0.03
p_x-p_x	(-1, -1)	0.030
d_x-d_x	(-1, 0)	0.030
d_x-p_y	(-1, 0)	-1.40
p_x-p_x	(-1, 0)	-0.03
p_y-d_x	(-1, 0)	0.010
d_x-d_x	(-1, 1)	0.030
p_x-d_x	(-1, 1)	-0.03
p_x-p_y	(-1, 1)	-0.66
d_x-d_x	(0, -2)	-0.01
p_x-p_x	(0, -2)	0.010
d_x-d_x	(0, -1)	0.030
d_x-p_y	(0, -1)	-0.03
p_x-p_x	(0, -1)	0.030
p_y-p_x	(0, -1)	0.660
d_x-d_x	(0, 0)	10.87
d_x-p_y	(0, 0)	1.400
p_x-p_x	(0, 0)	8.110
p_y-d_x	(0, 0)	1.400
p_y-p_y	(0, 0)	8.110
d_x-p_x	(0, 1)	-0.01
p_x-d_x	(0, 1)	1.400
p_x-p_y	(0, 1)	0.660
p_y-p_y	(0, 1)	-0.03
p_x-d_x	(0, 2)	0.010
p_y-p_y	(0, 2)	-0.01
d_x-p_x	(1, -1)	-0.03
p_y-d_x	(1, -1)	0.030
p_y-p_y	(1, -1)	0.030
d_x-p_x	(1, 0)	0.030
p_x-d_x	(1, 0)	0.030
p_y-d_x	(1, 0)	-1.40
p_y-p_y	(1, 0)	0.030
p_x-d_x	(1, 1)	-0.03
p_y-d_x	(1, 1)	0.030
d_x-d_x	(2, 0)	-0.01
p_y-p_y	(2, 0)	0.010

TABLE II. (*Continued.*)

Orbitals	Vector	Amplitude
d_x-p_y	(-2,0)	-0.01
d_x-d_x	(-1,-1)	0.030
d_x-p_y	(-1,-1)	0.030
p_y-p_y	(-1,-1)	0.030
d_x-p_x	(-1,0)	0.030
p_x-d_x	(-1,0)	0.030
p_x-p_y	(-1,0)	0.660
p_y-p_y	(-1,0)	0.030
d_x-p_y	(-1,1)	0.030
p_x-p_x	(-1,1)	0.030
p_y-p_y	(-1,1)	0.030
d_x-p_x	(0,-2)	0.010
p_y-p_y	(0,-2)	-0.01
d_x-p_x	(0,-1)	1.400
p_x-d_x	(0,-1)	-0.01
p_y-d_x	(0,-1)	-0.03
p_y-p_y	(0,-1)	-0.03
d_x-p_x	(0,0)	-1.40
p_x-d_x	(0,0)	-1.40
p_x-p_y	(0,0)	-0.66
p_y-p_x	(0,0)	-0.66
d_x-d_x	(0,1)	0.030
d_x-p_y	(0,1)	-0.03
p_x-p_x	(0,1)	0.030
p_y-d_x	(0,1)	-0.03
d_x-d_x	(0,2)	-0.01
p_x-p_x	(0,2)	0.010
d_x-d_x	(1,-1)	0.030
p_x-p_x	(1,-1)	0.030
p_y-p_x	(1,-1)	-0.66
d_x-d_x	(1,0)	0.030
d_x-p_y	(1,0)	0.010
p_x-p_x	(1,0)	-0.03
p_y-p_x	(1,0)	0.660
d_x-d_x	(1,1)	0.030
p_x-p_x	(1,1)	0.030
p_y-p_y	(1,1)	0.030
p_y-d_x	(2,0)	-0.01
p_y-p_y	(2,2)	0.000

TABLE III. Three-band model Hamiltonian parameters obtained by LDA downfolding for NCCO. The vector connecting the two different unit cells is shown, and the two orbitals connected by the hopping as well.

Orbitals	Vector	Amplitude
d_x-p_y	(-2, 0)	-0.01
d_x-d_x	(-1, -1)	0.020
d_x-p_y	(-1, -1)	0.050
p_y-p_y	(-1, -1)	0.030
d_x-p_x	(-1, 0)	0.050
p_x-d_x	(-1, 0)	0.050
p_x-p_y	(-1, 0)	0.540
p_y-p_y	(-1, 0)	0.210
d_x-p_y	(-1, 1)	0.050
p_x-p_x	(-1, 1)	0.030
p_y-p_x	(-1, 1)	-0.01
d_x-p_x	(0, -2)	0.010
d_x-d_x	(0, -1)	-0.07
d_x-p_y	(0, -1)	-0.05
p_x-p_x	(0, -1)	0.210
p_y-p_x	(0, -1)	0.540
d_x-d_x	(0, 0)	2.450
d_x-p_y	(0, 0)	1.160
p_x-p_x	(0, 0)	0.840
p_y-d_x	(0, 0)	1.160
p_y-p_y	(0, 0)	0.840
d_x-p_x	(0, 1)	-0.02
p_x-d_x	(0, 1)	1.160
p_x-p_y	(0, 1)	0.540
p_y-p_y	(0, 1)	-0.05
p_x-d_x	(0, 2)	0.010
d_x-p_x	(1, -1)	-0.05
p_x-p_y	(1, -1)	-0.01
p_y-p_x	(1, -1)	-0.54
d_x-d_x	(1, 0)	-0.07
d_x-p_y	(1, 0)	0.020
p_x-p_x	(1, 0)	-0.05
p_y-p_x	(1, 0)	0.540
d_x-d_x	(1, 1)	0.020
p_x-p_x	(1, 1)	0.030
p_y-p_y	(1, 1)	0.030
p_y-d_x	(2, 0)	-0.01
p_y-d_x	(-2, 0)	-0.01
d_x-p_x	(-1, -1)	-0.05

TABLE III. (*Continued.*)

Orbitals	Vector	Amplitude
p_x-p_x	(-1,-1)	0.030
d_x-d_x	(-1,0)	-0.07
d_x-p_y	(-1,0)	-1.16
p_x-p_x	(-1,0)	-0.05
p_y-d_x	(-1,0)	0.020
d_x-d_x	(-1,1)	0.020
p_x-d_x	(-1,1)	-0.05
p_x-p_y	(-1,1)	-0.54
p_y-p_y	(-1,1)	0.030
p_x-d_x	(0,-2)	0.010
d_x-p_x	(0,-1)	1.160
p_x-d_x	(0,-1)	-0.02
p_y-d_x	(0,-1)	-0.05
p_y-p_y	(0,-1)	-0.05
d_x-p_x	(0,0)	-1.16
p_x-d_x	(0,0)	-1.16
p_x-p_y	(0,0)	-0.54
p_y-p_x	(0,0)	-0.54
d_x-d_x	(0,1)	-0.07
d_x-p_y	(0,1)	-0.05
p_x-p_x	(0,1)	0.210
p_y-d_x	(0,1)	-0.05
d_x-p_x	(0,2)	0.010
d_x-d_x	(1,-1)	0.020
p_x-p_x	(1,-1)	0.030
p_y-d_x	(1,-1)	0.050
p_y-p_y	(1,-1)	0.030
d_x-p_x	(1,0)	0.050
p_x-d_x	(1,0)	0.050
p_y-d_x	(1,0)	-1.16
p_y-p_y	(1,0)	0.210
p_x-d_x	(1,1)	-0.05
p_y-d_x	(1,1)	0.050
d_x-p_y	(2,0)	-0.01
p_y-p_y	(2,2)	0.000

- ¹V. J. Emery, *Phys. Rev. Lett.* **58**, 2794 (1987).
- ²C. M. Varma, S. Schmitt-Rink, and E. Abrahams, *Solid State Commun.* **62**, 681 (1987).
- ³C. Weber, A. Lauchli, F. Mila, and T. Giamarchi, *Phys. Rev. Lett.* **102**, 017005 (2009).
- ⁴C. Lubritto, K. Rosciszewski, and A. M. Oles, *J. Phys.: Condens. Matter* **8**, 11053 (1996).
- ⁵W. Weber, *Z. Phys. B: Condens. Matter* **70**, 323 (1988).
- ⁶F. C. Zhang and T. M. Rice, *Phys. Rev. B* **37**, 3759 (1988).
- ⁷L. F. Feiner, J. H. Jefferson, and R. Raimondi, *Phys. Rev. B* **53**, 8751 (1996).
- ⁸W. Ku, T. Berlijn, and C. C. Lee, *Phys. Rev. Lett.* **104**, 216401 (2010).
- ⁹A. K. McMahan, J. F. Annett, and R. M. Martin, *Phys. Rev. B* **42**, 6268 (1990).
- ¹⁰M. S. Hybertsen, E. B. Stechel, M. Schluter, and D. R. Jennison, *Phys. Rev. B* **41**, 11068 (1990).
- ¹¹J. Zaanen, G. A. Sawatzky, and J. W. Allen, *Phys. Rev. Lett.* **55**, 418 (1985).
- ¹²*Perspectives in Many-Particle Physics*, edited by R. A. Broglia, J. R. Schrieffer, and P. F. Bortignon (North-Holland, Amsterdam, 1994), pp. 95–125.
- ¹³G. Kotliar, P. A. Lee, and N. Read, *Physica C* **153-155**, 538 (1988).
- ¹⁴M. Grilli, B. G. Kotliar, and A. J. Millis, *Phys. Rev. B* **42**, 329 (1990).
- ¹⁵Ju H. Kim, K. Levin, and A. Auerbach, *Phys. Rev. B* **39**, 11633 (1989).
- ¹⁶L. F. Feiner, M. Grilli, and C. Di Castro, *Phys. Rev. B* **45**, 10647 (1992).
- ¹⁷S. Caprara and M. Grilli, *Phys. Rev. B* **49**, 6971 (1994).
- ¹⁸J. Schmalian, G. Baumgärtel, and K.-H. Bennemann, *Solid State Commun.* **86**, 119 (1993).
- ¹⁹R. Raimondi, C. Castellani, M. Grilli, Y. Bang, and G. Kotliar, *Phys. Rev. B* **47**, 3331 (1993).
- ²⁰M. Grilli and C. Castellani, *Phys. Rev. B* **50**, 16880 (1994).
- ²¹G. Kotliar, *Int. J. Mod. Phys. B* **5**, 341 (1991).
- ²²A. Georges, G. Kotliar, W. Krauth, and M. J. Rozenberg, *Rev. Mod. Phys.* **68**, 13 (1996).
- ²³G. Kotliar, S. Y. Savrasov, K. Haule, V. S. Oudovenko, O. Parcollet, and C. A. Marianetti, *Rev. Mod. Phys.* **78**, 865 (2006).
- ²⁴Th. Maier, M. Jarrell, Th. Pruschke, and M. H. Hettler, *Rev. Mod. Phys.* **77**, 1027 (2005).
- ²⁵P. Sahebsara and D. Sénéchal, *Phys. Rev. Lett.* **97**, 257004 (2006).
- ²⁶G. Kotliar, *Eur. Phys. J. B* **11**, 27 (1999).
- ²⁷A. Georges, G. Kotliar, and W. Krauth, *Z. Phys. B: Condens. Matter* **92**, 313 (1993).
- ²⁸P. Lombardo, M. Avignon, J. Schmalian, and K. H. Bennemann, *Phys. Rev. B* **54**, 5317 (1996).
- ²⁹L. de' Medici, X. Wang, M. Capone, and A. J. Millis, *Phys. Rev. B* **80**, 054501 (2009).
- ³⁰A. Comanac, L. de' Medici, M. Capone, and A. J. Millis, *Nat. Phys.* **4**, 287 (2008).
- ³¹C. Weber, K. Haule, and G. Kotliar, *Phys. Rev. B* **78**, 134519 (2008).
- ³²C. Weber, K. Haule, and G. Kotliar, *Nat. Phys.* **6**, 574 (2010).
- ³³M. M. Korshunov, V. A. Gavrichkov, S. G. Ovchinnikov, I. A. Nekrasov, E. E. Kokorina, and Z. V. Pchelkina, *J. Phys.: Condens. Matter* **19**, 486203 (2007).
- ³⁴A. J. Millis, A. Zimmers, R. P. S. M. Lobo, N. Bontemps, and C. C. Homes, *Phys. Rev. B* **72**, 224517 (2005).
- ³⁵A. Macridin, M. Jarrell, T. Maier, and G. A. Sawatzky, *Phys. Rev. B* **71**, 134527 (2005).
- ³⁶X. Wang, E. Gull, L. de' Medici, M. Capone, and A. J. Millis, *Phys. Rev. B* **80**, 045101 (2009).
- ³⁷M. J. Rozenberg, G. Kotliar, and H. Kajueter, *Phys. Rev. B* **54**, 8452 (1996).
- ³⁸B. Kyung, V. Hankevych, A. M. Dare, and A. M. S. Tremblay, *Phys. Rev. Lett.* **93**, 147004 (2004).
- ³⁹T. Das, R. S. Markiewicz, and A. Bansil, *Phys. Rev. B* **81**, 174504 (2010).
- ⁴⁰R. S. Markiewicz and A. Bansil, *Phys. Rev. B* **75**, 020508 (2007).
- ⁴¹T. Das, R. Markiewicz, and A. Bansil, [arXiv:0807.4257](https://arxiv.org/abs/0807.4257) (unpublished).
- ⁴²PWSCF in QUANTUM ESPRESSO Package, (2007) <http://www.pwscf.org/>
- ⁴³D. Vanderbilt, *Phys. Rev. B* **41**, 7892 (1990).
- ⁴⁴I. Souza, N. Marzari, and D. Vanderbilt, *Phys. Rev. B* **65**, 035109 (2001).
- ⁴⁵A. A. Mostofi, J. R. Yates, Y.-S. Lee, I. Souza, D. Vanderbilt, and N. Marzari, *Comput. Phys. Commun.* **178**, 685 (2008).
- ⁴⁶M. M. Korshunov, V. A. Gavrichkov, S. G. Ovchinnikov, I. A. Nekrasov, Z. V. Pchelkina, and V. I. Anisimov, *Phys. Rev. B* **72**, 165104 (2005).
- ⁴⁷All calculations have been carried out at temperature $T=89$ K when not specified.
- ⁴⁸P. Werner, A. Comanac, L. de Medici, M. Troyer, and A. J. Millis, *Phys. Rev. Lett.* **97**, 076405 (2006).
- ⁴⁹K. Haule and G. Kotliar, *Phys. Rev. B* **76**, 104509 (2007).
- ⁵⁰A. Amaricci *et al.* (unpublished).
- ⁵¹P. K. Mang, O. P. Vajk, A. Arvanitaki, J. W. Lynn, and M. Greven, *Phys. Rev. Lett.* **93**, 027002 (2004).
- ⁵²F. Borsa, P. Carreta, J. H. Cho, F. C. Chou, Q. Hu, D. C. Johnston, A. Lascialfari, D. R. Torgeson, R. J. Gooding, N. M. Salem, and K. J. E. Vos, *Phys. Rev. B* **52**, 7334 (1995).
- ⁵³N. D. Mermin and H. Wagner, *Phys. Rev. Lett.* **17**, 1133 (1966).
- ⁵⁴M. Civelli, M. Capone, S. S. Kancharla, O. Parcollet, and G. Kotliar, *Phys. Rev. Lett.* **95**, 106402 (2005).
- ⁵⁵D. Senechal, P.-L. Lavertu, M.-A. Marois, and A.-M. S. Tremblay, *Phys. Rev. Lett.* **94**, 156404 (2005).
- ⁵⁶E. Gull, M. Ferrero, O. Parcollet, A. Georges, and A. Millis, [arXiv:1007.2592](https://arxiv.org/abs/1007.2592) (unpublished).
- ⁵⁷G. Sordi, A. Amaricci, and M. J. Rozenberg, *Phys. Rev. B* **80**, 035129 (2009).
- ⁵⁸For better comparison with experiments, we mapped the ordered state calculations $A^a(\mathbf{K}, \omega)$ to the paramagnetic Brillouin zone, see Appendix A.
- ⁵⁹N. P. Armitage, F. Ronning, D. H. Lu, C. Kim, A. Damascelli, K. M. Shen, D. L. Feng, H. Eisaki, Z. X. Shen, P. K. Mang, N. Kaneko, M. Greven, Y. Onose, Y. Taguchi, and Y. Tokura, *Phys. Rev. Lett.* **88**, 257001 (2002).
- ⁶⁰H. Matsui, K. Terashima, T. Sato, T. Takahashi, S. Wang, H. Yang, H. Ding, T. Uefuji, and K. Yamada, *J. Phys. Chem. Solids* **67**, 249 (2006).
- ⁶¹M. Ikeda, T. Yoshida, A. Fujimori, M. Kubota, K. Ono, Y. Kaga, T. Sasagawa, and H. Takagi, *Phys. Rev. B* **80**, 184506 (2009).
- ⁶²B. Moritz, F. Schmitt, W. Meevasana, S. Johnston, E. M. Motoyama, M. Greven, D. H. Lu, C. Kim, R. T. Scalettar, Z.-X.

- Shen, and T. P. Devereaux, *New J. Phys.* **11**, 093020 (2009).
- ⁶³N. P. Armitage, D. H. Lu, C. Kim, A. Damascelli, K. M. Shen, F. Ronning, D. L. Feng, P. Bogdanov, Z. X. Shen, Y. Onose, Y. Taguchi, Y. Tokura, P. K. Mang, N. Kaneko, and M. Greven, *Phys. Rev. Lett.* **87**, 147003 (2001).
- ⁶⁴T. Yoshida, X. J. Zhou, K. Tanaka, W. L. Yang, Z. Hussain, Z.-X. Shen, A. Fujimori, S. Sahrakorpi, M. Lindroos, R. S. Markiewicz, A. Bansil, S. Komiyama, Y. Ando, H. Eisaki, T. Kakeshita, and S. Uchida, *Phys. Rev. B* **74**, 224510 (2006).
- ⁶⁵I. A. Nekrasov, E. Z. Kuchinskii, and M. V. Sadovskii, *J. Phys. Chem. Solids* **69**, 3269 (2008).
- ⁶⁶T. Valla, T. E. Kidd, W. G. Yin, G. D. Gu, P. D. Johnson, Z. H. Pan, and A. V. Fedorov, *Phys. Rev. Lett.* **98**, 167003 (2007).
- ⁶⁷C. T. Chen, L. H. Tjeng, J. Kwo, H. L. Kao, P. Rudolf, F. Sette, and R. M. Fleming, *Phys. Rev. Lett.* **68**, 2543 (1992).
- ⁶⁸X. Wang, L. de Medici, and A. J. Millis, *Phys. Rev. B* **81**, 094522 (2010).
- ⁶⁹D. C. Peets, D. G. Hawthorn, K. M. Shen, Y.-J. Kim, D. S. Ellis, H. Zhang, S. Komiyama, Y. Ando, G. A. Sawatzky, R. Liang, D. A. Bonn, and W. N. Hardy, *Phys. Rev. Lett.* **103**, 087402 (2009).
- ⁷⁰E. S. Božin and S. J. L. Billinge, *Phys. Rev. B* **72**, 174427 (2005).
- ⁷¹P. S. Cornaglia and A. Georges, *Phys. Rev. B* **75**, 115112 (2007).
- ⁷²N. L. Wang, G. Li, D. Wu, X. H. Chen, C. H. Wang, and H. Ding, *Phys. Rev. B* **73**, 184502 (2006).
- ⁷³T. Xiang, H. G. Luo, D. H. Lu, K. M. Shen, and Z. X. Shen, *Phys. Rev. B* **79**, 014524 (2009).
- ⁷⁴S. Uchida, T. Ido, H. Takagi, T. Arima, Y. Tokura, and S. Tajima, *Phys. Rev. B* **43**, 7942 (1991).
- ⁷⁵J. M. Tomczak, *Eur. Phys. Lett.* **86**, 37004 (2009).
- ⁷⁶A. Zimmers, J. M. Tomczak, R. P. S. M. Lobo, N. Bontemps, C. P. Hill, M. C. Barr, Y. Dagan, R. L. Greene, A. J. Millis, and C. C. Homes, *Europhys. Lett.* **70**, 225 (2005).
- ⁷⁷Y. Onose, Y. Taguchi, K. Ishizaka, and Y. Tokura, *Phys. Rev. Lett.* **87**, 217001 (2001).
- ⁷⁸S. Lupi, M. Ortolani, A. Lucarelli, A. Perla, P. Calvani, P. Masselli, N. Kikugawa, and T. Fujita, *J. Supercond.* **17**, 131 (2004).
- ⁷⁹Y. Onose, Y. Taguchi, K. Ishizaka, and Y. Tokura, *Phys. Rev. B* **69**, 024504 (2004).
- ⁸⁰T. Startseva, T. Timusk, A. V. Puchkov, D. N. Basov, H. A. Mook, M. Okuya, T. Kimura, and K. Kishio, *Phys. Rev. B* **59**, 7184 (1999).
- ⁸¹N. Bontemps, R. P. S. M. Lobo, A. F. Santander-Syro, and A. Zimmers, *Ann. Phys.* **321**, 1547 (2006).
- ⁸²A. M.-S. Tremblay (private communication).
- ⁸³R. S. Markiewicz, S. Sahrakorpi, M. Lindroos, H. Lin, and A. Bansil, *Phys. Rev. B* **72**, 054519 (2005).
- ⁸⁴S. Basak, T. Das, H. Lin, J. Nieminen, M. Lindroos, R. S. Markiewicz, and A. Bansil, *Phys. Rev. B* **80**, 214520 (2009).
- ⁸⁵P. Phillips, *Rev. Mod. Phys.* **82**, 1719 (2010).
- ⁸⁶P. Phillips and M. Jarrell, [arXiv:1003.3412](https://arxiv.org/abs/1003.3412) (unpublished).
- ⁸⁷P. Phillips, T. Choy, and R. Leigh, *Rep. Prog. Phys.* **72**, 036501 (2009).
- ⁸⁸O. Matsumoto, A. Utsuki, A. Tsukada, H. Yamamoto, T. Manabe, and M. Naito, *Phys. Rev. B* **79**, 100508 (2009).
- ⁸⁹O. Matsumoto, A. Utsuki, A. Tsukada, H. Yamamoto, T. Manabe, and M. Naito, *Physica C* **468**, 1148 (2008).
- ⁹⁰M. Naito, O. Matsumoto, A. Utsuki, A. Tsukada, H. Yamamoto, and T. Manabe, *J. Phys.* **108**, 012037 (2008).